Coumarin 6 Appended Terpyridine-Based Cyclometalated Ir(III) Photocatalysts for NADH Oxidation and ROS-Mediated Anticancer Activity

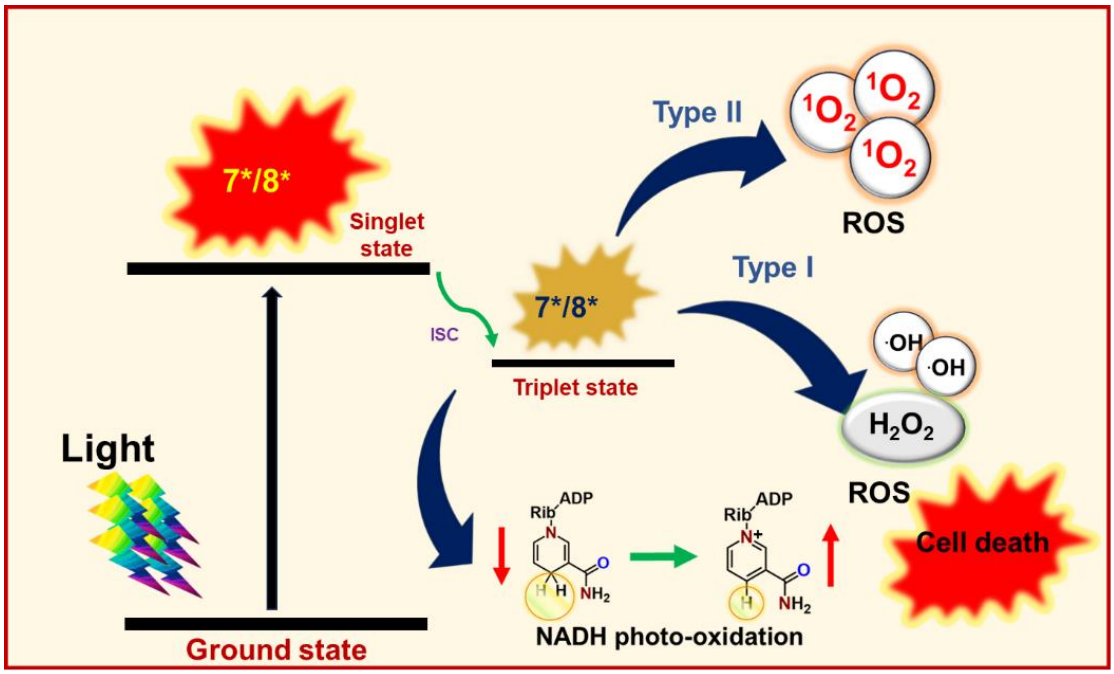

Published in *Inorg. Chem. Commun.* **2025**, *175*, 114184.

4.1. Abstract

In this chapter we developed and evaluated two novel coumarin 6 conjugated Ir(III) photocatalysts, [Ir(CO6)(Ph-tpy)Cl]Cl (**7**) and [Ir(CO6)(An-tpy)Cl]Cl (**8**) (CO6 = Coumarin 6, Ph-tpy = 4'-phenyl-2,2':6',2''-terpyridine, An-tpy = 4'-anthracenyl-2,2':6',2''-terpyridine), for application in cancer therapy. Upon green light irradiation (525 nm, 50.2 J cm^{-2}), **7** and **8** effectively catalyzed NADH oxidation with turnover frequencies (TOFs) ranging from 840 to 1100 h^{-1} in phosphate-buffered saline. Additionally, these photocatalysts (**7** and **8**) generated reactive oxygen species (ROS), including $^1O_2$, H_2O_2, and $^{\bullet}OH$, through type I and type II mechanisms. **7** and **8** exhibited significant toxicity against human breast (MCF-7) and cervical (HeLa) cancer cells, with **8** demonstrating enhanced anticancer activity upon light activation. Notably, both photocatalysts (**7** and **8**) showed minimal dark toxicity toward non-cancerous human embryonic kidney (HEK-293) cells. The selectivity index (SI = Dark IC_{50} in normal cells / Dark IC_{50} in cancer cells) for **7** and **8** reached up to 22, highlighting their preferential activity in cancer cells. Mechanistic studies in MCF-7 cells with the most effective photocatalyst, **8**, revealed that light exposure increased ROS production and induced mitochondrial depolarization and apoptosis *via* caspase 3/7 activation.

4.2. Introduction

We have Synthesized three cyclometallated Ir(III) photocatalysts in **Chapter III**, *viz*., $[Ir(CO6)_2(phen)]Cl$ **(4)**, $[Ir(CO6)_2(dppz)]Cl$ **(5)**, and $[Ir(CO6)_2(aip)]Cl$ **(6)** where, CO6 = Coumarin 6, phen = 1,10-phenanthroline, dppz = dipyrido[3,2-a:2',3'-c]phenazine, and aip = 2-(anthracen-9-yl)-1H-imidazo[4,5-f][1,10]phenanthroline.[1] **4-6** not only exhibited

green light absorption properties but also demonstrated green light-induced impressive NADH oxidation turnover frequencies, surpassing those of previously reported Ir(III)-based photocatalysts. Furthermore, they demonstrated significant cytotoxicity against cancer cells under visible light irradiation. However, despite the photocatalysts showing good NADH oxidation turnover frequencies, there is still room to further enhance the TOFs by the suitable design of the Ir(III) photocatalysts. In **Chapter III**, we introduced two coumarin 6 ligands in combination with a bidentate N,N donor ligand, which shifted the light activation wavelength of Ir(III) photocatalysts in the green region and successfully yielded good TOF for NADH oxidation. Considering the importance of NADH in photocatalytic cancer therapy, in this chapter, we aim to improve the NADH oxidation TOFs by replacing N,N donor ligand with N,N,N-donor ligand and by attaching only one coumarin 6 moiety. We introduced an anthracene moiety to enhance the photosensitizing ability and improve the lipophilicity of **8**. Additionally, the extended conjugation in phenyl terpyridine and anthracene terpyridine ligands was anticipated to enhance the electron-accepting ability and reduction potential of the photocatalysts, thereby improving the photocatalytic NADH oxidation efficacy of **7** and **8**.[2,3] Herein, we present the synthesis, characterization, green light-induced in-solution ROS generation, and NADH oxidation, visible light-induced cytotoxicity, and intracellular change in concentration ratio of NAD^+/NADH properties of two cyclometallated Ir(III)-based photocatalysts *viz.*, [Ir(CO6)(Ph-tpy)Cl]Cl (**7**) and [Ir(CO6)(An-tpy)Cl]Cl (**8**) (Figure 4.1).[4] Notably, our findings revealed (i) very high NADH photo-oxidation TOFs for **8**, even higher than those we reported in **Chapter III** under 525 nm green light, (ii) good anticancer activities of **8** under dark, (iii) augmentation of anticancer activities of **8** after light exposure, and (iv)

synergistic type-I and type-II ROS generation mechanisms for light-activated augmentation of anticancer activities.

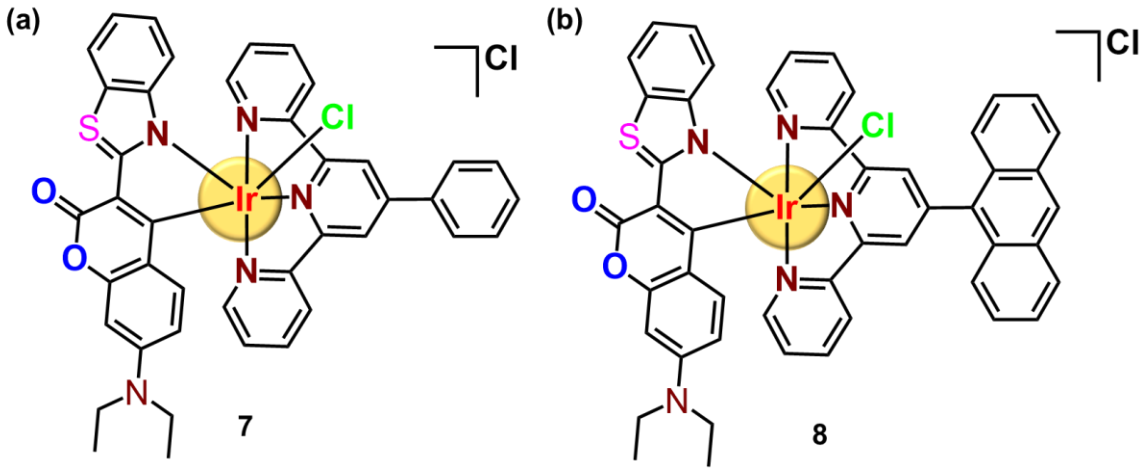

Figure 4.1: Chemical Structures of **7** (a) and **8** (b).

4.3. Results and Discussion

4.3.1. Synthesis and Characterization

Photocatalysts **7** and **8** were synthesized by reacting [Ir(Ph/An-tpy)Cl_3] with Coumarin 6 in ethylene glycol under heating conditions (Scheme 4.1).[5] The resulting photocatalysts (**7** and **8**) were purified using column chromatography in neutral alumina using methanol and ethyl acetate (1:99, v/v) as eluents. The synthesized photocatalysts (**7** and **8**) were thoroughly characterized *via* HR-MS, ^{1}H and ^{13}C NMR spectroscopy, UV-Vis. spectroscopy, and emission measurements. In high-resolution mass spectra, molecular ion peaks were observed at m/z = 886.2027 and 986.2212 corresponding to the $[M]^{+}$ ion for **7** and **8**, respectively (Figures 4.2a, b).

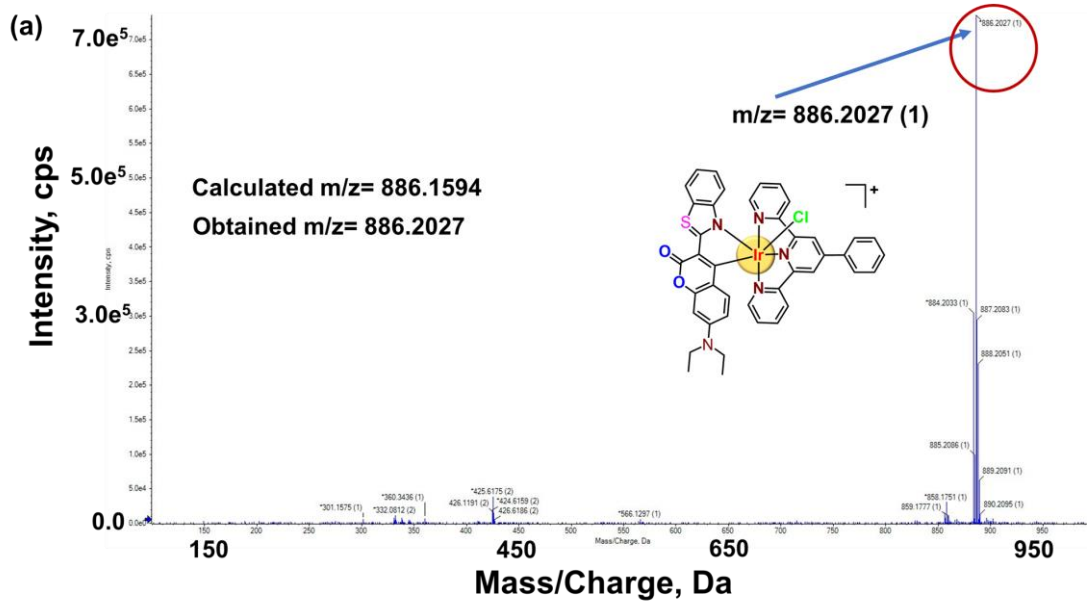

Figure 4.2: (a) HR-MS spectrum of **7** in methanol showing $[M]^+$ ion peak.

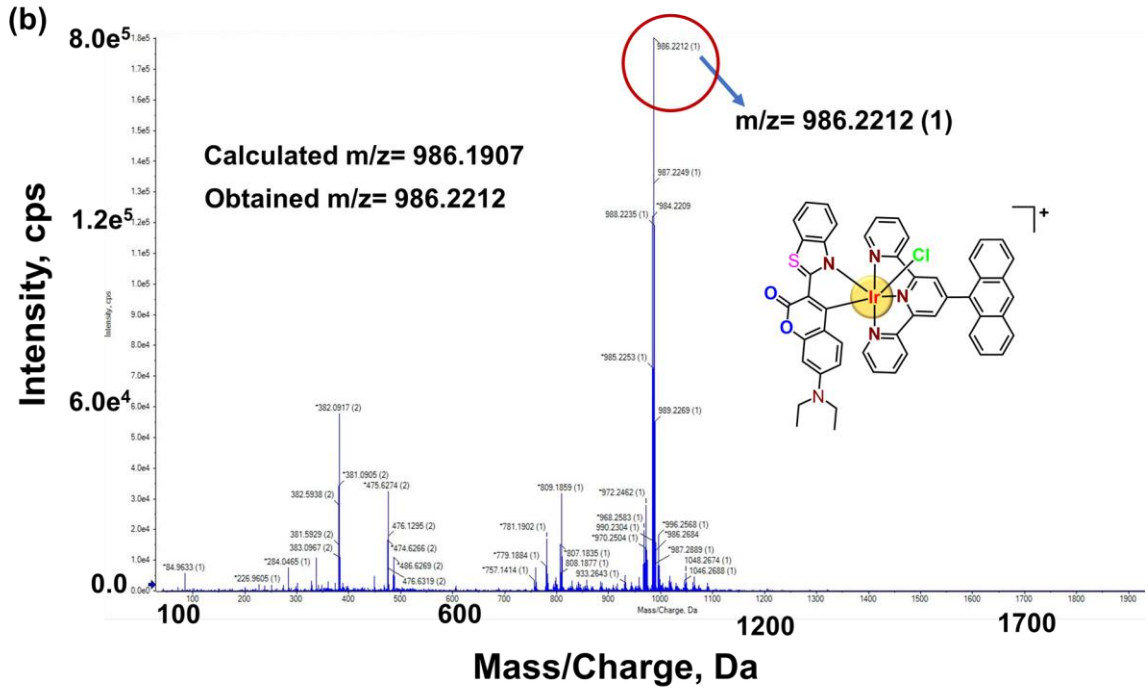

Figure 4.2: (b) HR-MS spectrum of **8** in methanol showing $[M]^+$ ion peak.

The ^{1}H and ^{13}C NMR spectra of **7** and **8** were recorded in DMSO-d_6 (Figures 4.3a, b and 4.4a, b). The ^{1}H NMR spectra revealed well-resolved signals that supported the proposed structure. The peaks observed in the aromatic region (δ ~ 6.0–9.5 ppm) correspond to the aromatic protons of the coumarin 6 and terpyridine-based ligand, consistent with the expected integration and chemical shifts (Figures 4.3a, b).[5-8] A distinct triplet at δ = 0.97 ppm was assigned to the terminal methyl (–CH_3) protons of the ethyl group of -NCH_2CH_3 unit of coumarin 6, while a corresponding quartet around δ = 3.3 ppm confirmed the presence of the adjacent methylene (–CH_2–) protons.[7,8] Characteristic signals for aromatic carbons were observed in the range of δ = 110–160 ppm (Figures 4.4a, b). The methyl carbon of the ethyl group appeared upfield at around δ = 12.83 ppm, while the methylene carbon resonated at δ = 44.99 ppm, both consistent with a typical ethyl substituent.[7,8]

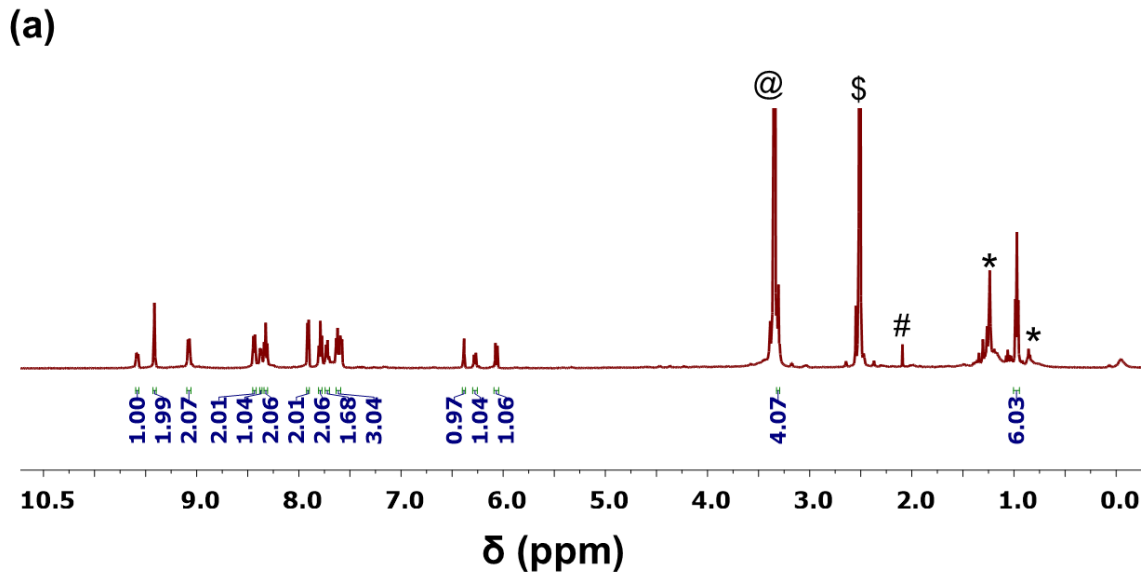

Figure 4.3: (a) ^{1}H NMR spectra of **7** in DMSO-d_6 (500 MHz). (Residual solvent peaks: $^{@}H_2O$ in DMSO-d_6 $^{\$}$DMSO-$d_6$, $^{\#}$acetone, *n-hexane).

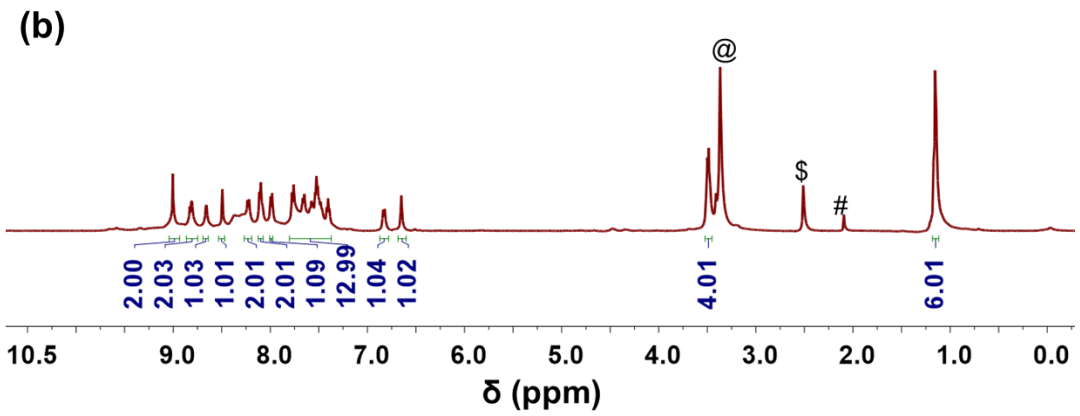

Figure 4.3: (b) ^{1}H NMR spectra of **8** in DMSO-d_6 (500 MHz). (Residual solvent peaks: $^{@}H_2O$ in DMSO-d_6 $^{\$}$DMSO-$d_6$, $^{\#}$acetone).

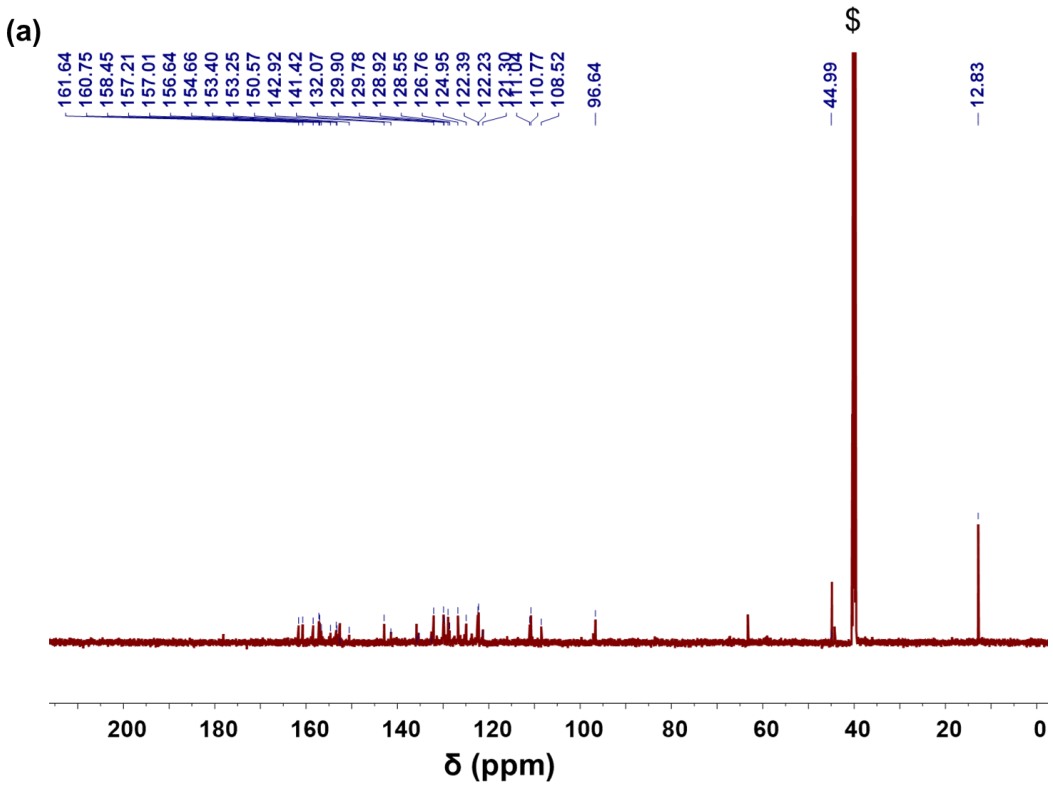

Figure 4.4: (a) $^{13}C\{^{1}H\}$ NMR spectra of **7** in DMSO-d_6 (125 MHz). (Residual solvent peaks: $^{\$}$DMSO-$d_6$).

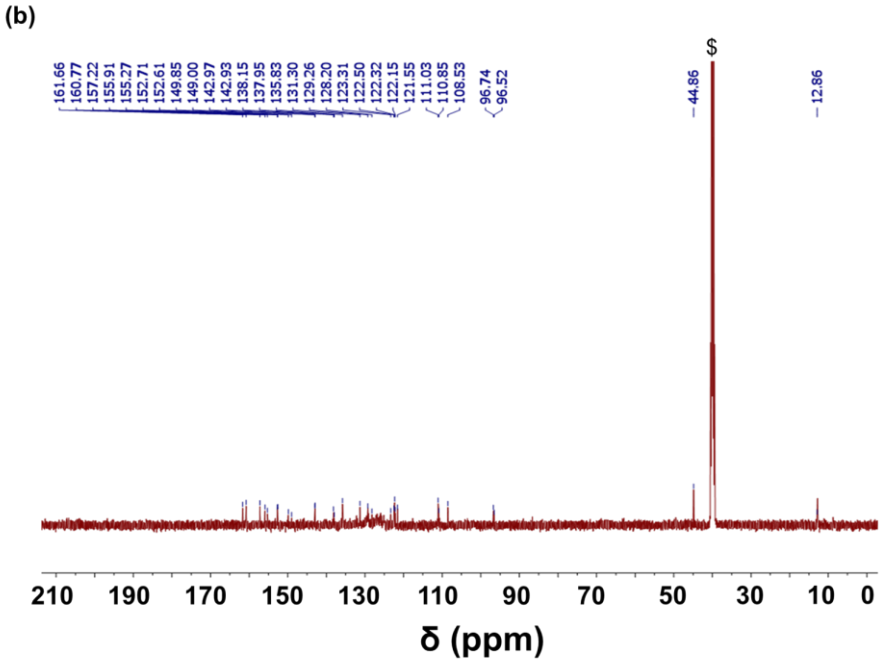

Figure 4.4: (b) $^{13}C\{^{1}H\}$ NMR spectra of **8** in DMSO-d_6 (125 MHz). (Residual solvent peaks: $^{\$}$DMSO-$d_6$).

The UV-Vis. study of **7** and **8** showed an MLCT band at 400-450 nm,[1,8] and bands between 470-550 nm corresponded to the intra-ligand π→π* transitions of coumarin 6 (Figure 4.5a).[1,8] A similar result was also reported by Zhao *et al.* and Luo *et al.*, where coumarin 6-based

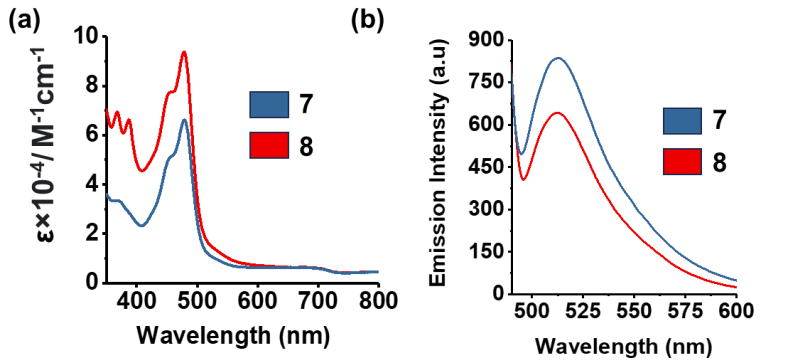

Figure 4.5: (a) Absorption spectra of **7** and **8** in DMSO:PBS (0.5:99.5, v/v). (b) Emission spectra of **7** and **8** (20 μM each) in DMSO:PBS (0.5:99.5, v/v) [λ_{ex} = 460 nm].

photocatalysts displayed the occurrence of ^{1}IL/^{1}MLCT in the range of 400-550.[9,10] Bonnet *et al.* have pointed out that for photo-activated cancer therapy, it is a preferred strategy to bathochromically shift the absorption maximum as much as possible of any phototherapeutic agent and then activate the compound with the red-shifted excitation wavelengths compared to the absorption maximum of the photocatalysts.[11] Therefore, the presence of the extended tail in the green light region in the UV-Vis. spectra of the photocatalysts (**7** and **8**) indicated that **7** and **8** might show NADH oxidation and ROS generation, and simultaneously anticancer activity under green light[1,5,12] **7** and **8** exhibited green emission when excited at 460 nm in DMSO:PBS (0.5:99.5, v/v) (Figure 4.5b), suggesting that **7** and **8** can also be useful for cellular localization studies.[1,7,8]

The lipophilicity (log*P*) of **7** and **8** was evaluated using the "shake-flask" method by measuring their distribution coefficient between the water and octanol phases.[1,13] The log $P_{o/w}$ value of **7** and **8** was obtained to be 1.61±0.24 and 2.20±0.30, respectively (Figure 4.6a), which is well within the range of a drug candidate.[14] The photostability of **7** and **8** under green light

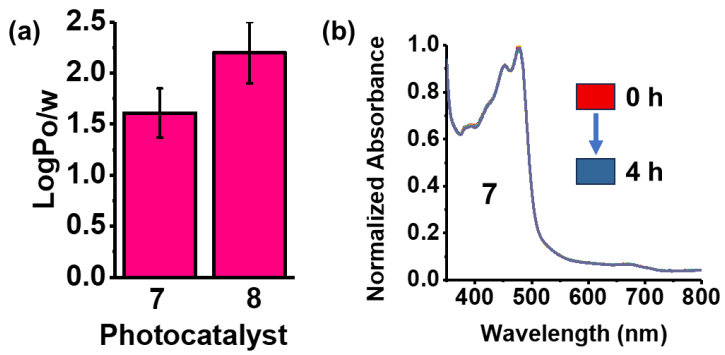

Figure 4.6: (a) Octanol-water partition coefficients of photocatalysts **7** and **8**. (b) The UV-Vis. absorption spectra representing the green light stability of photocatalyst **7** at various time intervals in DMSO:PBS (0.5:99.5, v/v).

irradiation (525 nm, 50.2 J cm^{-2}) was studied in DMSO:PBS (0.5:99.5, v/v). No significant changes were observed in UV-Vis. spectra over time upon light exposure (Figures 4.6b, c), indicating the photostability of **7** and **8**. Further, to confirm the aqueous stability of **7** and **8**, we have compared the UV-Vis. spectra of **7** with its dehalogenated species, generated using $AgNO_3$ treatment (Figure 4.6d). The dehalogenated analogue of **7** exhibited a bathochromic shift of *ca*. 10 nm, indicating the formation of dehalogenated species (Figure 4.6d).[15,16] These results suggested that **7** and **8** remained stable under aqueous conditions and do not readily form their dehalogenation species. This stability is crucial for photo-pharmacological efficacy and photocatalytic activities, ensuring sustained activity under light irradiation.[1,4-8,17,18] The high photostability of **7** and **8**, combined with their green light absorption ability, made the photocatalysts promising candidates for photoactivated anticancer applications, considering the possible capacity of **7** and **8** to catalyze NADH oxidation and generate ROS under green light.[1,4,5,8,17]

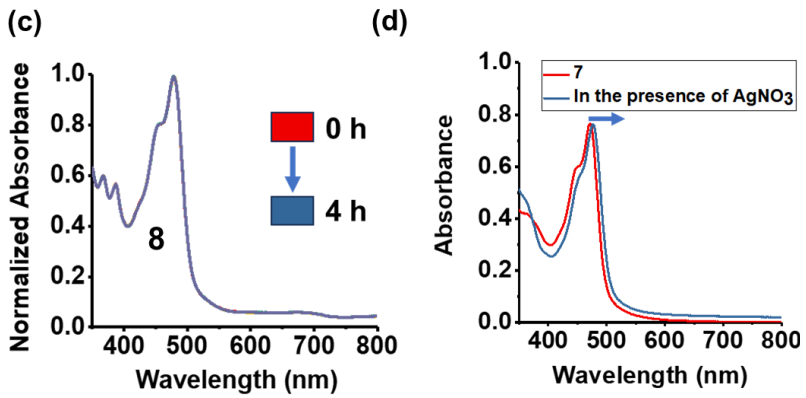

Figure 4.6: (c) The UV-Vis. absorption spectra representing the green light stability of photocatalyst **8** at various time intervals in DMSO:PBS (0.5:99.5, v/v). (d) The UV-Vis. absorption spectra of **7** and its dehalogenated species generated by $AgNO_3$ treatment.

4.3.2. DFT Calculation

To gain insights into the electronic properties of **7** and **8**, DFT calculations at the B3LYP/LANL2DZ level were performed using Gaussian 16.[19] The optimized geometries of both photocatalysts revealed a distorted octahedral coordination environment around the central Ir(III) center. An analysis of the frontier molecular orbitals (FMOs) indicated that the HOMO of **7** is largely localized on the coumarin 6 moiety. In contrast, the LUMO was delocalized over the Ir(III) ion and the Ph-tpy ligand. (Figure 4.7). For photocatalyst **8**, HOMO was based on both the Ir(III) center and the coumarin 6 moiety, whereas the LUMO was primarily localized on the terpyridine moiety (Figure 4.7). Both the photocatalysts (**7** and **8**) showed a narrow energy gap ($\Delta E_g \leq 2.0$ eV) between the HOMO and LUMO, indicating that they are probably going to function as efficient photosensitizers when exposed to visible light.[1,5]

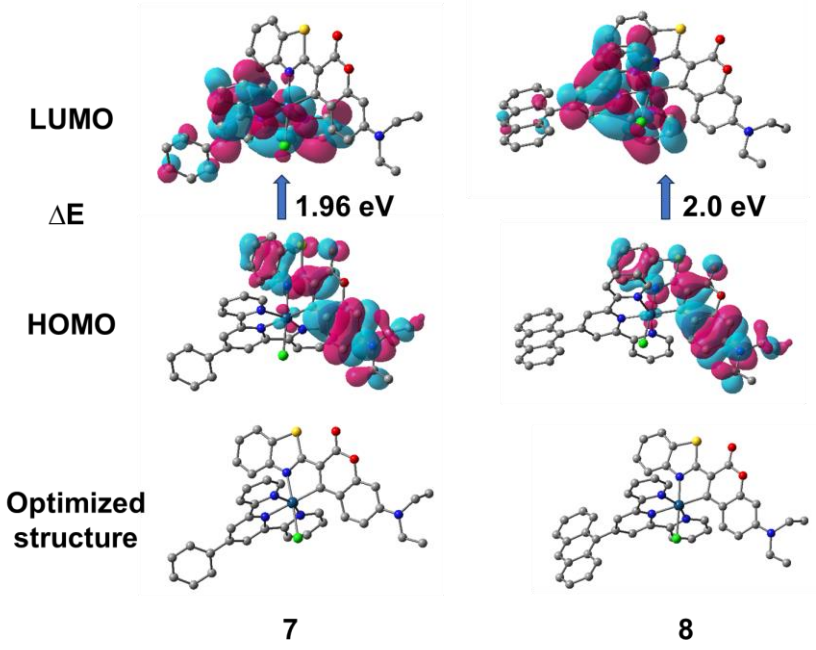

Figure 4.7: The optimized structures and HOMO, LUMO of **7** and **8**.

Time-Dependent DFT (TD-DFT) computations were performed at the B3LYP/LANL2DZ level to examine the excited state characteristics of **7** and **8**.[1,5] Tables 4.1 and Table 4.2 present the computed lowest 10 vertical singlet–singlet/triplet transition energies. The minimum $\Delta E_{S0\text{-}T1}$ energy required for the conversion of $^3O_2$ to $^1O_2$ is 0.98 eV,[20] and the calculated $\Delta E_{S0\text{-}T1}$ energy of **7** and **8** was 2.03 eV and 1.70 eV respectively, i.e. >0.98 eV (Figure 4.8), suggesting that these photocatalysts (**7** and **8**) at the T_1 state have enough energy to convert $^3O_2$ into $^1O_2$. $^1O_2$ generation was also confirmed with DPBF, a singlet oxygen detection probe (see In-solution ROS Generation **section 4.3.4**).

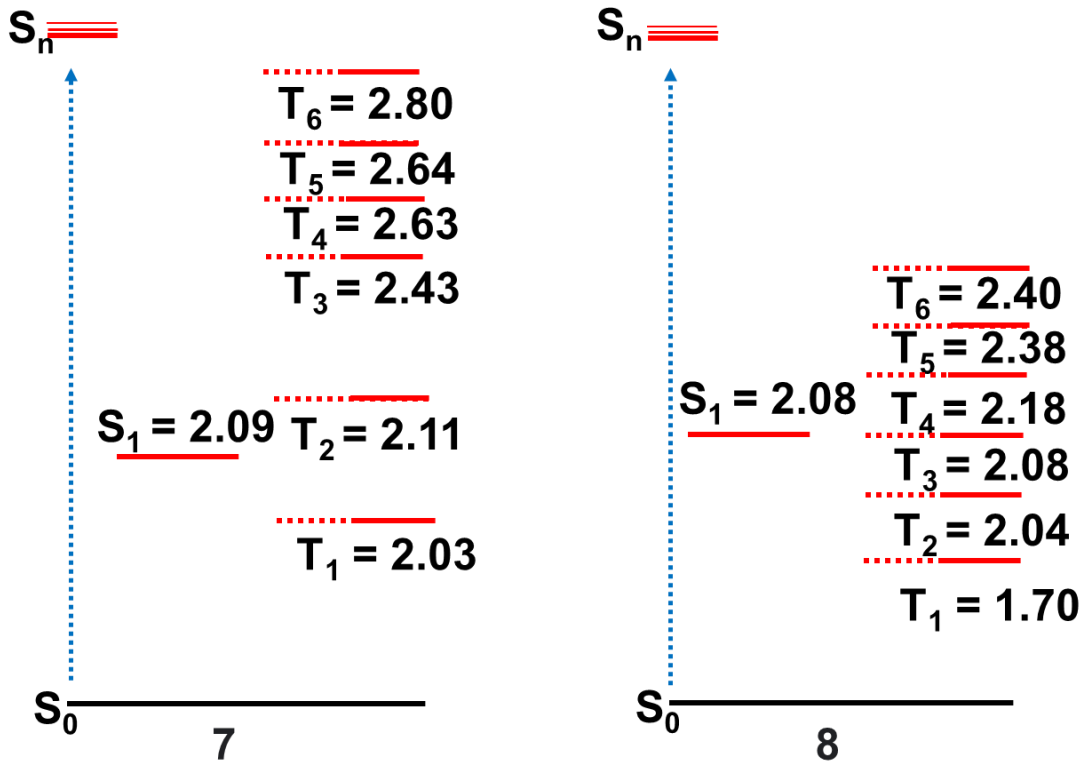

Figure 4.8: Vertical energy levels of the different electronic states of **7** and **8**, obtained from TD-B3LYP/LANL2DZ in water. All energy values are in eV.

Table 4.1: Energy (eV) of the lowest vertical 10 singlet–singlet ($S_0 \rightarrow S_n$; n = 1 to 10) transitions of **7** and **8** computed at the TD-B3LYP /LANL2DZ/6-31g* level of theory in water. The oscillator strengths are indicated in parentheses.

Singlet state	**Energy (eV) of the lowest vertical 10 singlet–singlet transition**	
	7	**8**
S1	2.0872 (0.0040)	2.0759 (0.0020)
S2	2.4410 (0.0005)	2.1743 (0.0735)
S3	2.7600 (0.0077)	2.4180 (0.0005)
S4	2.7835 (1.0125)	2.4247 (0.0011)
S5	3.0921 (0.0413)	2.7504 (0.0065)
S6	3.1683 (0.0003)	2.7834 (1.0014)
S7	3.2254 (0.0878)	2.9431 (0.0000)
S8	3.2930 (0.0037)	3.1060 (0.0006)
S9	3.3665 (0.0001)	3.1162 (0.0034)
S10	3.4074 (0.0007)	3.1498 (0.1853)

Table 4.2: Energy (eV) of the lowest vertical 10 singlet–triplet ($S_0 \rightarrow T_n$; n = 1 to 10) transitions of the **7** and **8** computed at the TD-B3LYP /LANL2DZ/6-31g* level of theory in water.

Triplet state	**Energy (eV) of the lowest vertical 10 singlet–triplet transition**	
	7	**8**
T_1	2.0319	1.7008
T_2	2.1075	2.0406
T_3	2.4308	2.0849
T_4	2.6302	2.1797
T_5	2.6445	2.3824
T_6	2.8035	2.4090
T_7	2.9158	2.6233
T_8	3.0730	2.7466
T_9	3.0938	2.8051
T_{10}	3.1642	2.9422

4.3.3. NADH Photo-oxidation

The photocatalytic potential of **7** and **8** for NADH oxidation was evaluated using UV-Vis. spectroscopy by monitoring the decrease in NADH absorbance at 339 nm.[1,4-8,17,18] The photocatalysts (**7** and **8**) significantly reduced the absorbance of NADH when exposed to

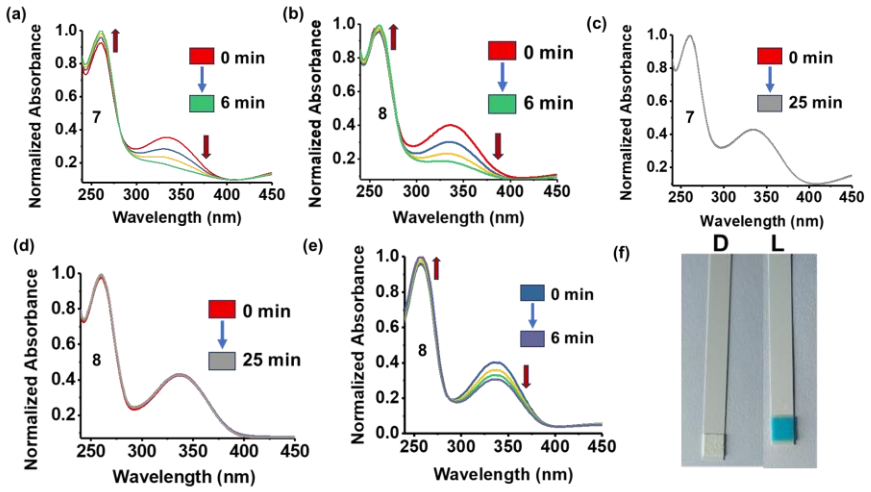

Figure 4.9: (a) and (b) represent green light (525 nm, 50.2 J cm^{-2}) induced NADH (150 µM) oxidation by **7** and **8**, respectively (1 µM each). Solvent: DMSO:PBS (0.5:99.5, v/v). (c) and (d) represent NADH (150 µM) oxidation by **7** and **8**, respectively (1 µM each) under dark conditions. Solvent: DMSO:PBS (0.5:99.5, v/v). (e) UV-Vis. spectra showing the green light (525 nm, 50.2 J cm^{-2}) induced NADH (150 µM) oxidation in the presence of **8** (1 µM) + GSH (50 µM). Solvent: DMSO:PBS (0.5:99.5, v/v). For (a), (b), and (e), the outcome of the results was expressed as mean ± SD. The statistical analysis was done by One-way ANOVA followed by Tukey's Post Hoc Test (n=3). (f) H_2O_2 generation was detected after 1 minute of green light irradiation (525 nm, 50.2 J cm^{-2}) to the **8** (1 µM) and NADH (150 µM) reaction mixture. Solvent: DMSO:PBS (0.5:99.5, v/v).

green light (525 nm, 50.2 J cm^{-2}) (Figures 4.9a, b). At the same time, the increase in absorbance of a characteristic peak around 265 nm demonstrated the generation of NAD^+ due to NADH photo-oxidation.[4-8] Notably, in the absence of light, **7** and **8** induced negligible changes in the NADH (150 μM) absorption spectrum over a 25-min incubation period (Figures 4.9c, d). As summarized in Table 4.3, **8** exhibited superior NADH photo-oxidation activity, achieving a TON of *ca.* 108.2±4.1 and a TOF of around 1084.6±39.4 h^{-1}. **7** exhibited TON and TOF of *ca.* 97.7±5.7 and 969.3±56.9 h^{-1}, respectively. These TOF values significantly surpass those reported for previously explored Ir(III) based photocatalysts, **Ir1** (33.6 h^{-1}), **Ir8** (126.4 h^{-1}), **Ir9** (735.1 h^{-1}), **Ir12** (270.6 h^{-1}), **Ir23** (16.9 h^{-1}), **Ir24** (42.8 h^{-1}), **Ir25** (414.2 h^{-1}) (Table 4.3).[5,6,12,21]Importantly, the TOF achieved in the case of **8** (TOF = 1084.6±39.4) is much higher than the TOF achieved by the highly active photocatalyst **6** (TOF = 1003.5±24.6) in **Chapter III**. These findings confirmed our hypothesis regarding improving photocatalytic activity by extending conjugation. Further, in order to understand the effect of GSH on NADH photooxidation TOF, we conducted a similar experiment in the presence of GSH.

In the presence of GSH, the NADH oxidation TON (*ca*. 81.1±4.0) and TOF (*ca*. 805.3±32.6 h^{-1}) of **8** were slightly reduced compared to those in the absence of GSH (TON = 108.2±4.2 and TOF = 1084.6±39.4 h^{-1}) (Figure 4.9e). This indicated that even in the presence of GSH, NADH might be the main target of the photocatalysts. The aforementioned findings showed that **7** and **8** are effective photocatalysts for NADH oxidation. It's interesting to note that the peroxide detection strip did not demonstrate any appreciable formation of H_2O_2 in the absence of light during NADH oxidation studies

(Figure 4.9f). But it demonstrated H_2O_2 generation in response to green light (525 nm, 50.2 J cm^{-2}) during NADH oxidation (Figure 4.9f). This suggested that H_2O_2 was produced *via* a type-I photocatalytic oxidation pathway involving NADH oxidation, as reported earlier by Sadler, Huang, and our group.[1,4-8,17,18]

Table 4.3: Comparison of TON and TOF of **7** and **8** with other reported Ir(III) photo-catalysts for NADH photo-oxidation.

Photocatalyst	**TON**	**TOF (h^{-1})**
7[a]	97.7±5.7	969.3±56.9
8[a]	108.2±4.2	1084.6±39.4
4[b]	17.0±2.5	621.4±90.6
5[b]	28.0±2.1	841.4±45.8
6[b]	66.9±1.6	1003.5±24.6
Ir1[c]	16.8	33.6
Ir8[d]	5.8	34.7
Ir9[d]	74.8	448.6
Ir12[e]	18.0	270.6
Ir23[f]	8.4	16.9
Ir24[f]	21.4	42.8

Ir25[f]	207.1	414.2
Ce6[f]	24.5	49

[a]TON and TOF of **7** and **8** (1 μM each) for photocatalytic oxidation of NADH (150 μM) in DMSO:PBS (0.5:99.5, v/v) solution, light source: 525 nm, 50.2 J cm^{-2}. [b]TONs and TOFs of **4-6** (2 μM each) for photocatalytic oxidation of NADH (240 μM) in DMSO:PBS (0.5:99.5, v/v) solution, light source: 525 nm, 50.2 J cm^{-2} (Taken from reference 1). [c]TON and TOFs for photocatalytic NADH oxidation (120 μM) by **Ir1** (3 μM) in (0.5:99.5, v/v) solution, light source: 463 nm, 8.9 J cm^{-2} (Taken from reference 6). [d]TON and TOFs for photocatalytic oxidation of NADH (150 μM) by photocatalysts (**Ir8** and **Ir9**) (1 μM) in PBS, light source: 525 nm, 49.26 mW/cm^2 (Taken from reference 5). [e]TON and TOFs for photocatalytic oxidation of NADH (100 μM) by **Ir12** (5 μM each) in water, light source: 635 nm, 145 mW cm^{-2} (Taken from reference 12). [f]TON and TOFs for photocatalytic oxidation of NADH (160 μM) by **Ir23-Ir25** (5 μM each) in PBS, light source: 465 nm, 1.2 J cm^{-2} (Taken from reference 21).

4.3.4. In-solution ROS Generation

The likelihood of **7** and **8** to produce $^1O_2$ was investigated by monitoring changes in the absorbance of DPBF.[22,23] When **7** and **8** were subjected to green light irradiation, the absorbance of DPBF decreased, indicating their propensity to generate $^1O_2$ (Figures 4.10a, b). As the irradiation time was increased, the photocatalysts' $^1O_2$ generation was also increased, as shown by the change in the absorbance *vs*. irradiation duration plot (Figure 4.10c). Further, when we exposed the DPBF solution (50 μM) (only as a control) to the

green light, no significant change in the absorbance was recorded (Figure 4.10d), confirming that the $^1O_2$ generation under light was due to **7** and **8**. In another experiment, we further studied the change in the absorbance of DPBF+**7**/**8** solution in the absence of light; the unchanged absorption intensity of DPBF reflected the necessity of light for $^1O_2$ generation (Figures 4.10e, f). Furthermore, the $^1O_2$ generation quantum yield (Φ_Δ) of each photocatalyst was determined

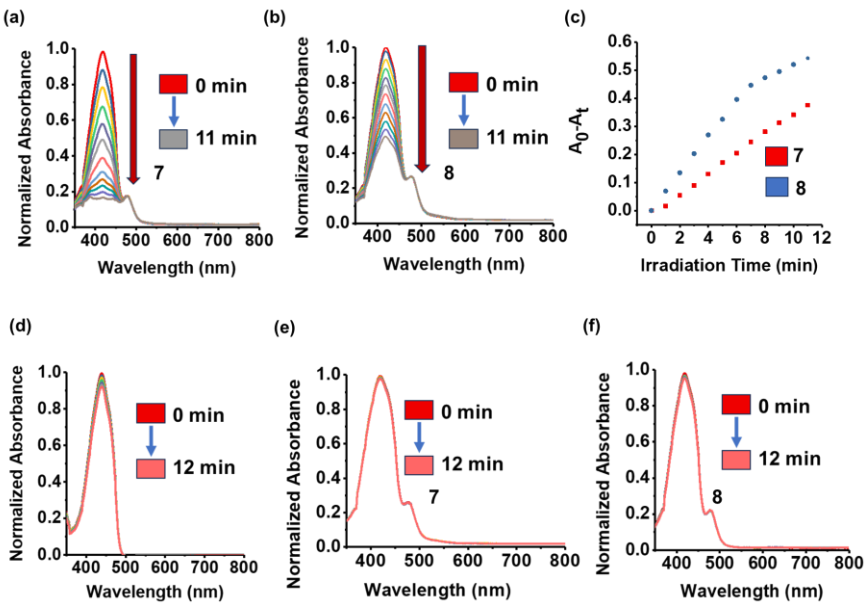

Figure 4.10: Absorbance changes of DPBF (50 µM) indicating $^1O_2$ generation by (a) **7** and (b) **8** (2 µM each) upon 525 nm light irradiation (50.2 J cm^{-2}). Solvent: DMSO:PBS (0.5:99.5, v/v). (c) Change in absorbance of DPBF (50 µM) *vs* irradiation time plot for **7** and **8** (2 µM each) upon 525 nm light (50.2 J cm^{-2}) irradiation indicated an increase in $^1O_2$ generation of photocatalysts with an increase in irradiation time. Solvent: DMSO:PBS (0.5:99.5, v/v). (d) No significant change in absorption spectra of DPBF (50 µM) in DMSO:PBS (0.5:99.5, v/v) under green light irradiation, representing green light (525 nm, 50.2 J cm^{-2}) stability of DPBF. The absorption spectra of DPBF (50 µM) in the presence of **7** (e) and **8** (f) (2 µM each) in DMSO:PBS (0.5:99.5, v/v) under dark conditions.

relative to $[Ru(bpy)_3]Cl_2$ (Φ_Δ = 0.22 in aq. DMSO) (Figure 4.11a).[1] The measured Φ_Δ values were 0.03 and 0.05 for **7** and **8**, respectively. The above observations suggested that **7** and **8** could act as photocatalysts cum photosensitizers for green-activated anticancer applications. Additionally, the MB probe was used to assess the photocatalysts' propensity to produce $^{\bullet}OH$ under green light (525 nm, 50.2 J cm^{-2}).[1,24] In a solution of methylene blue containing **7** or **8** in DMSO:PBS (0.5:99.5, v/v), the absorbance of MB between 650 and 700 nm gradually decreased with exposure to green light, as shown in Figures 4.11b and c. Moreover, to confirm the $^{\bullet}OH$ generation, we

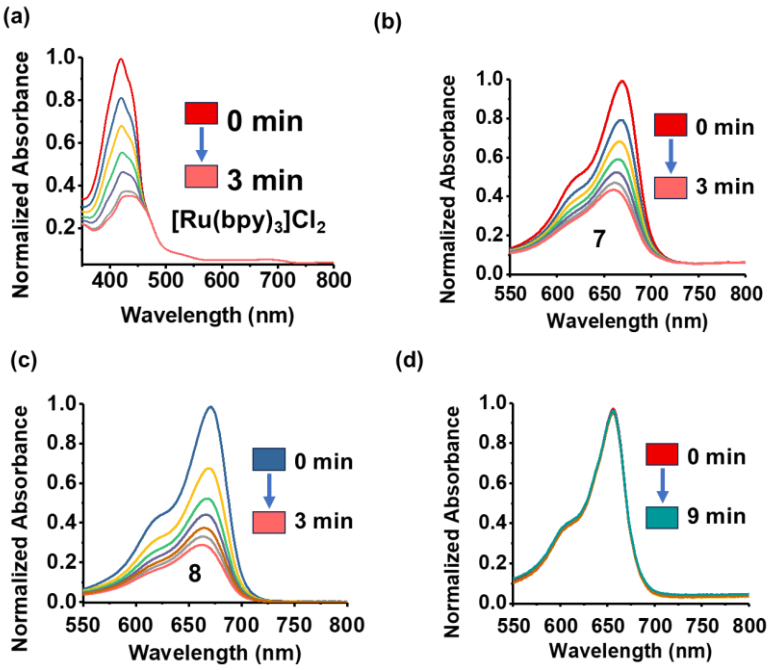

Figure 4.11: (a) Absorbance changes of DPBF (50 µM) in the presence of $[Ru(bpy)_3]Cl_2$ (2 µM) with respect to time upon 525 nm light irradiation. Solvent: DMSO:PBS (0.5:99.5, v/v). Absorbance changes of methylene blue (15 µM) in the presence of (b) **7** and (c) **8** (2 µM each), indicating $^{\bullet}OH$ generation under light irradiation (525 nm, 50.2 J cm^{-2}). Solvent: DMSO:PBS (0.5:99.5, v/v). (d) Absorption spectra of methylene blue (15 µM) in the presence of **8** (2 µM)+Light (525 nm, 50.2 J cm^{-2})+tert-butanol (8 µL). Solvent: DMSO:PBS (0.5:99.5, v/v).

have performed the MB degradation experiment in the presence of tert-butanol, a well-known •OH radical scavenger.[25,26] The obtained result (Figure 4.11d) displayed an insignificant decrease in the MB-based peak when MB+**8** was irradiated with green light in the presence of tert-butanol, suggesting that the observed decrease in MB-based peaks was specifically due to •OH generation. These findings suggested that the photocatalysts can produce •OH radicals. Thus, both type I (including NADH oxidation, H_2O_2, and •OH generation) and type II (using $^1O_2$ production) pathways might be used by **7** and **8** to exhibit photocytotoxicity. This finding is significant because most Ir(III) or Ru(II) photosensitizers have been demonstrated to function largely through the type II pathway for exhibiting anticancer effects.[27-29]

4.3.5. Cellular Toxicity

Photocatalysts **7** and **8** in an aqueous solution demonstrated green light-induced ROS production and NADH oxidation. Thus, it was hypothesized that **7** and **8** could be promising photoactivated anticancer metallodrug candidates. The MTT

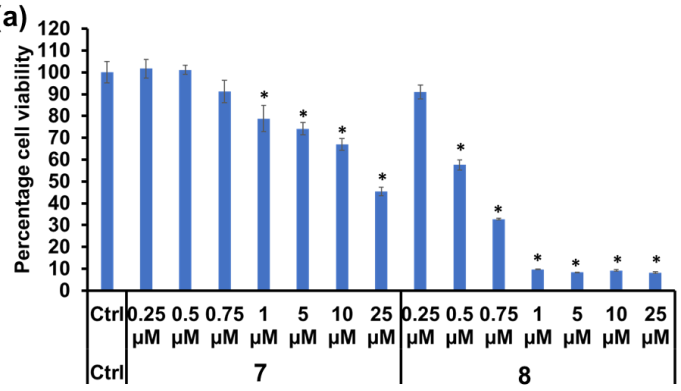

Figure 4.12: (a) Cell viability plots of **7** and **8** against MCF-7 cells under dark. The outcome of the results was expressed as mean ± SD (error bars are standard deviations). The statistical analysis was done by One-way ANOVA followed by Tukey's Post Hoc Test (n=3). Where * denotes statistically significant ($p<0.05$).

assay was used to evaluate their anticancer activity against MCF-7 and HeLa cancer cells in both dark and light conditions (Figures 4.12a, b and 4.13a, b).[30,31] MCF-7 and HeLa cells were selected as these cells are highly aggressive, adaptable to various experimental conditions, and have been widely used in drug screening and cancer research studies.[32,33] Interestingly, cell viability was reduced by **7** and **8** even in the dark (Figures 4.12a, 4.13a, Table 4.4), indicating their ability to kill cancer cells in the dark. More interestingly, the cancer cell-killing activities of **7** and **8** were enhanced after light exposure (Figures 4.12b, 4.13b, Table 4.4). Photocatalyst **8**'s IC_{50} against MCF-7 and HeLa cancer cells were *ca*. 0.3 µM and 1.0 µM, respectively, under visible light exposure (400-700 nm, 5.0 J cm^{-2}) (Table 4.4). Whereas, under similar light conditions, photocatalyst **7** against MCF-7 and HeLa cancer cells demonstrated IC_{50} values of *ca*. 22.1±1.9 and 23.1±1.4 µM, respectively (Table 4.4). **8** showed roughly 23-70 times more phototoxicity than **7** in HeLa and MCF-7, respectively. In comparison to **7** (PI ~1), the phototoxicity index (PI = Dark IC_{50}/Light IC_{50}) of **8** was higher (2.0–7.0). Additionally,

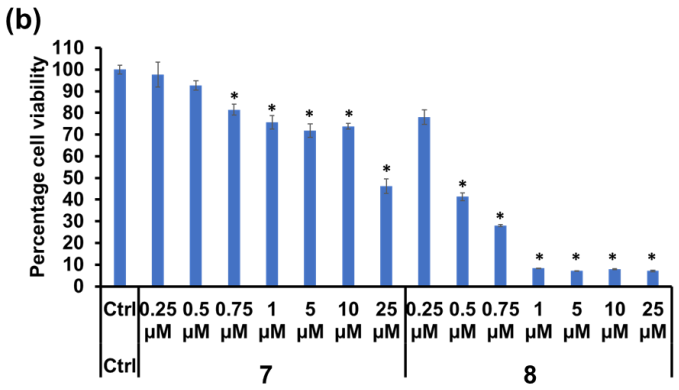

Figure 4.12: (b) Cell viability plots of **7** and **8** against MCF-7 cells under light irradiation (400-700 nm, 5.0 J cm^{-2}). The outcome of the results was expressed as mean ± SD (error bars are standard deviations). The statistical analysis was done by One-way ANOVA followed by Tukey's Post Hoc Test (n=3). Where * denotes statistically significant ($p<0.05$).

photocatalyst **8** showed higher phototoxicity with respect to the other Ir(III)-based green light photocatalysts such as **Ir8** and **Ir9** (Table 4.4).[5] Under light irradiation, photocatalyst **8** demonstrated superior cytotoxicity against HeLa cells, with an IC_{50} value lower than those of photocatalysts **4** (2.5 ± 0.1 µM) and **5** (1.6 ± 0.1 µM), as reported in **Chapter III**. Moreover, its activity was comparable to that of the highly potent photocatalyst **6** (IC_{50} = 0.9 ± 0.1 µM) as reported in **Chapter III**, further underscoring the therapeutic potential of **8** under photoactivation. Further, the cytotoxicity of **7** and **8** was also tested against the HEK-293 normal cell line in both dark and light conditions (Figures 4.14a, b, Table 4.4). As evidence of their safety profile, **7** and **8** showed no appreciable toxicity to HEK-293 cells with IC_{50} values of *ca.* >25.0 µM and 13.4±1.3 µM, respectively, in the dark. The aforementioned finding highlighted that **8** targeted cancer cells with a high selectivity index (SI = Dark IC_{50} in normal cells /Dark IC_{50} in cancer cells), SI = 22.0 in MCF-7 cells.

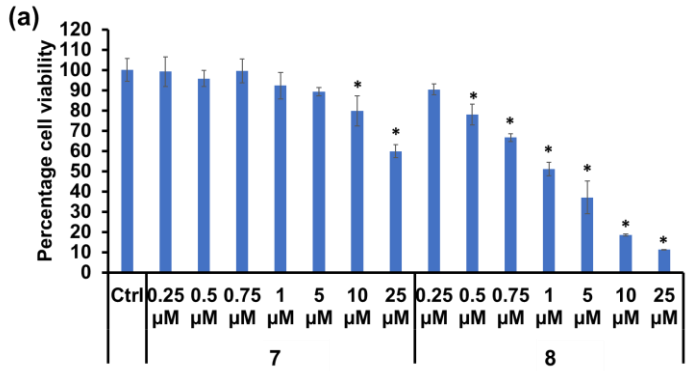

Figure 4.13: (a) Cell viability plots of **7** and 8 against HeLa cells under dark. The outcome of the results was expressed as mean ± SD (error bars are standard deviations). The statistical analysis was done by One-way ANOVA followed by Tukey's Post Hoc Test (n=3). Where * denotes statistically significant ($p<0.05$).

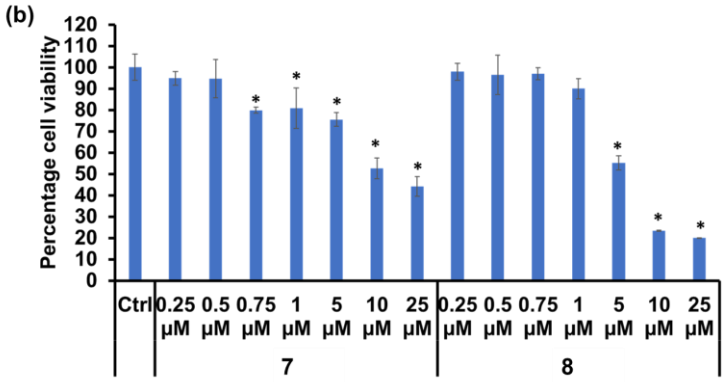

Figure 4.13: (b) Cell viability plots of **7** and **8** against HeLa cells under light irradiation (400-700 nm, 5.0 J cm^{-2}). The outcome of the results was expressed as mean ± SD (error bars are standard deviations) of the three independent repeated experiments. The statistical analysis was done by One-way ANOVA followed by Tukey's Post Hoc Test (n=3). Where * denotes statistically significant ($p<0.05$).

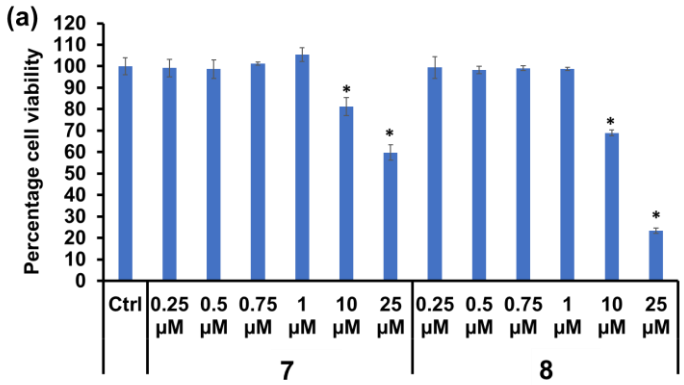

Figure 4.14: (a) Cell viability plots of **7** and **8** against HEK-293 cells under dark conditions. The outcome of the results was expressed as mean ± SD (error bars are standard deviations) of the three independent repeated experiments. The statistical analysis was done by One-way ANOVA followed by Tukey's Post Hoc Test (n=3). Where * denotes statistically significant ($p<0.05$).

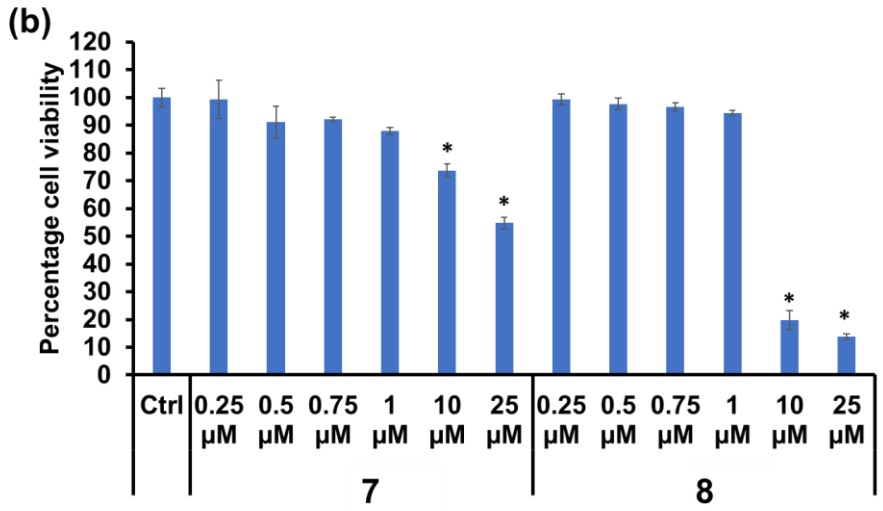

Figure 4.14: (b) Cell viability plots of **7** and **8** against HEK-293 cells under light irradiation (400-700 nm, 5.0 J cm^{-2}). The outcome of the results was expressed as mean ± SD (error bars are standard deviations) of the three independent repeated experiments. The statistical analysis was done by One-way ANOVA followed by Tukey's Post Hoc Test (n=3). Where * denotes statistically significant ($p<0.05$).

Table 4.4: IC_{50} (µM) values of **7**, **8**, and some selected Ir(III)-based photo-catalysts.

Photocatalyst	MCF-7				HeLa				HEK-293	
	Dark	Light	PI	SI	Dark	Light	PI	SI	Dark	Light
7[a]	23.5 ±2.7	22.1±1.9	1.1	>1.0	>25.0	23.1±1.4	1.1	>1.0	>25.0	>25.0
8[a]	0.6± 0.1	0.3±0.1	2.0	22.3	7.0±0.2	1.0±0.1	7.0	1.9	13.4±1.3	7.9±0.4

4[b]					>50.0	2.5 ±0.1				
5[b]					44.4±2.1	1.6±0.1				
6[b]					43.7±1.8	0.9±0.1				
Ir8[c]					20.0	13.9	1.4			
Ir9[c]					47.9	2.7	17.7			
Cisplatin[c]					16.5	25.3				
5-ALA[c]					>1000	151.1	6.6			

[a]Cells were incubated with **7**/**8** for 6 h, followed by light exposure (400–700 nm, 5.0 J cm^{-2}) over 2 min. Recovery after irradiation: 18 h. For the dark group, the light irradiation step was absent. [b]Cells were incubated with **4**/**5**/**6** for 4 h, followed by light exposure (400–700 nm, 10 J cm^{-2}) over 1 h. Recovery after irradiation: 43 h. For the dark group, the light irradiation step was absent (**Chapter III** photocatalysts). [c]Cells were incubated with **Ir8**/**Ir9**/**5-ALA**/**cis-platin** for 8 h, followed by light exposure (525 nm, 29.56 J cm^{-2}) over 30 min. Recovery after irradiation: 40 h. For the dark group, the light irradiation step was absent (taken from reference 5).

4.3.6. Cellular Localization and In-cell NADH Oxidation

The cellular uptake and localization of any potential drug are critical parameters.[1,5] The cellular uptake of **8** in MCF-7 cells was determined using its inherent green emission. The obtained result revealed the significant accumulation of **8** in the cytosol of MCF-7 cells within 6 h of incubation (Figure 4.15a). This cytosolic localization suggested that **8** may disrupt the MMP by generating ROS and oxidizing NADH.[34] Considering the ability of **8** to photo-oxidize NADH in solution, the effect of **8** (0.5 μM, *ca*. light IC_{50}) treatment on the levels of NADH and NAD^+ was monitored in MCF-7 cells under dark and light conditions (Figure 4.15b). The results indicated that **8** treatment alone significantly decreased the NADH/NAD^+ ratio as compared to the control, untreated dark group over a period of 24 h, corroborating the toxicity of **8** itself in the dark. The light-exposed group did not show any significant change in the NADH/NAD^+ as compared to the untreated dark control group (Figure 4.15b). Remarkably, light irradiation of **8**-treated cells led to a further

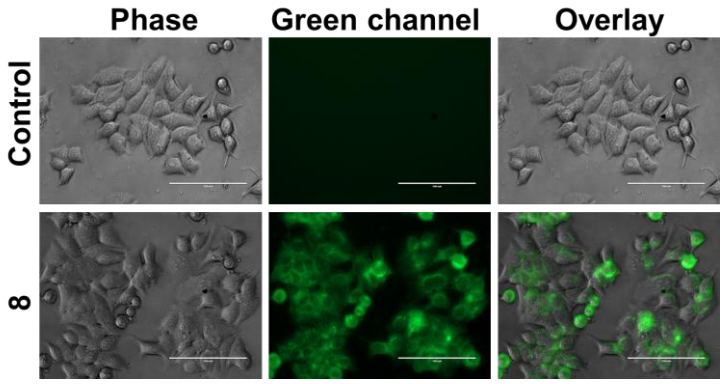

Figure 4.15: (a) Fluorescence microscopy images showing the cytosolic localization of **8** in MCF-7 cells. Cells were incubated with **8** (at its light IC_{50} concentration, 6 h). Scale bar: 100 μm. The experiment was repeated three times independently with similar results.

significant decrease in the NADH/NAD^+ ratio (Figure 4.15b). Thus, this result confirmed the NADH photo-oxidation ability of **8** within the cancer cellular environment.

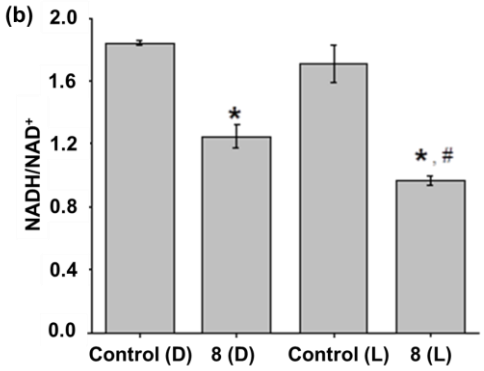

Figure 4.15: (b) The plot displays the ratio of NADH/NAD^+ in MCF-7 cells treated with **8** (0.5 μM) using the spectrophotometric analysis (L = Light, D = Dark). One set of cells was exposed to visible light (400-700 nm, 5.0 J cm^{-2}) after 4 h of incubation with **8**, while the other set was kept continuously in the dark. The total incubation period following the addition of the photocatalyst was 24 h. The results are presented as mean ± SD (n = 2). * $p< 0.05$ as compared to the dark control group by student T-test; # $p< 0.05$ as compared to the light control group by student T-test.

4.3.7. In-cell ROS Generation

As discussed above, **8** can produce $^1O_2$ and $^{\bullet}OH$ when exposed to light, suggesting that **8** may produce ROS in cancer cells through type I and type II pathways.[4-8] Using DCFH-DA as a ROS probe (for the theory of DCFH-DA assay, see **Chapter II**, **section 2.3.6**),[35,36] we evaluated the intracellular ROS production capacity of **8** (at its light IC_{50} concentration) in MCF-7 cancer cells (Figure 4.16a). As illustrated in Figure 4.16a, the results showed that **8** (at its light IC_{50} concentration) within MCF-7 cells generated a considerable amount of

ROS in the dark. ROS generation by **8** in the dark might be another reason for its dark toxicity. Interestingly, there was a significant increase in the ROS generation ability of **8** in response to light, as indicated by more intense intracellular green fluorescence in the **8** (at its light IC_{50} concentration)+Light-treated group. The notable increase in the ROS generation under light compared to the dark is one of the reasons for the higher toxicity of **8** after light activation.

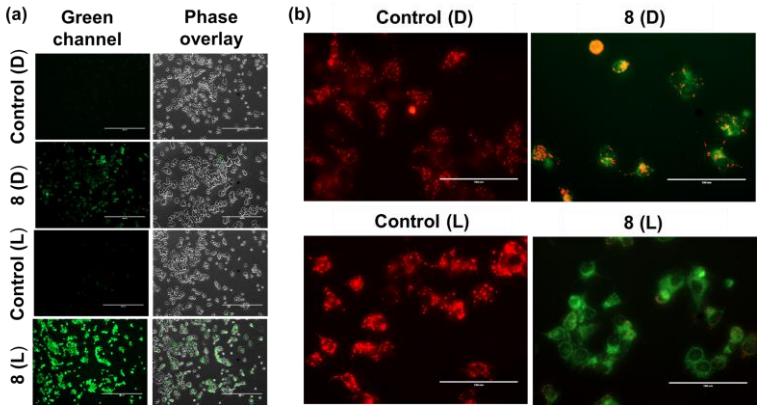

Figure 4.16: (a) Detection of intracellular ROS generation in MCF-7 cells induced by **8** (at its light IC_{50} concentration) under exposure to visible light (400-700 nm, 5.0 J cm^{-2}) or under dark conditions using the DCFH-DA probe (L = Light, D = Dark). Incubation time with **8**: 6 h, Light irradiation (400-700 nm, 5.0 J cm^{-2}) for 2 min. Recovery after irradiation: 18 h. For the dark group, the light irradiation step was absent. Scale bar: 400 μm. (b) Change in the MMP of **8** (at its light IC_{50} concentration) treated MCF-7 cells as monitored by JC-1 assay after light exposure or in the dark (L = Light, D = Dark). Incubation time with **8**: 6 h, Light irradiation (400-700 nm, 5.0 J cm^{-2}) for 2 min. Recovery after irradiation: 18 h. For the dark group, the light irradiation step was absent. Scale bar: 100 μm. For both (a) and (b), the experiment was repeated three times independently with similar results.

4.3.8. Depolarization of Mitochondrial Membrane Potential (MMP)

According to earlier research, transition metal photocatalysts that produce ROS affected mitochondrial membrane potential (MMP) ($\Delta\Psi_m$) and caused cancer cells to undergo apoptosis.[4-8] Thus, the effect of **8** on the MMP of MCF-7 cells was evaluated using the JC-1 assay (for the theory of the JC-1 assay, see **Chapter II** section **2.3.7**).[37,38] As depicted in Figure 4.16b, under dark conditions, **8** (at its light IC_{50} concentration)-treated MCF-7 cells showed red and green fluorescence, suggesting a change in MMP. The change in MMP became more evident (from bright green fluorescence) after light irradiation, indicating a sharp decrease and alteration in MMP. The study suggested that the **8** (at its light IC_{50} concentration)+Light combination affects MMP more compared to **8** only, most likely as a result of more ROS production and NADH oxidation under light.

4.3.9. Cell Death Mechanism

The ROS generation and change in MMP by **8** prompted us to investigate the cell death mechanism. The process of cell death was identified using the Hoechst/PI dual staining (Figure 4.17) (for the theory of Hoechst/PI dual staining, see **Chapter II**, **section 2.3.8**).[39,40] When MCF-7 cells were exposed to **8** (at its light IC_{50} concentration)+Light, as demonstrated in Figure 4.17, they displayed red emission with propidium iodide (PI) and blue emission with Hoechst. The overlay images showed pink emission, indicating an apoptotic cell death mechanism. However, when **8** was present alone, only a very weak red fluorescence was observed (Figure 4.17), suggesting that **8** had reduced toxicity in the dark.

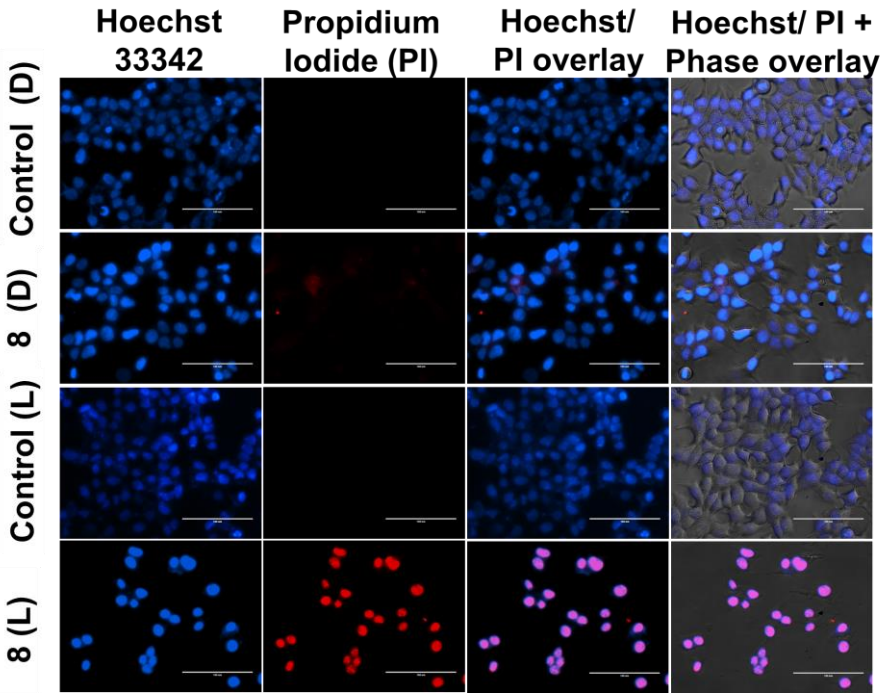

Figure 4.17: Hoechst and Propidium Iodide staining revealed that **8** (at its light IC_{50} concentration) caused light-activated apoptotic cell death in MCF-7 cells (L = Light, D = Dark). Incubation time with **8**: 6 h, light irradiation (400-700 nm, 5.0 J cm^{-2}) for 2 min. Recovery after irradiation: 18 h. For the dark group, the light irradiation step was absent. Scale bar: 100 μm. The experiment was repeated three times independently with similar results.

The sequential activation of caspases is a hallmark of apoptosis.[41,42] Thus, the possibility of caspase 3/7 activation in MCF-7 cells after treatment with **8** (at its light IC_{50} concentration) under light or in the dark was studied by caspase 3/7 green detection reagent and SYTOX.[41,42] The results (Figure 4.18) demonstrated that treatment of MCF-7 cells with **8** (at its light IC_{50} concentration) in the dark led to activation of caspase 3/7. Upon exposure to light, caspase 3/7 activation increased significantly compared to the dark

(Figure 4.18). These findings indicate that **8** (at its light IC_{50} concentration), when combined with light irradiation, markedly enhances the expression of the key apoptosis executor caspase 3/7, thereby promoting cell death. Overall, considering the above consequences, it can be concluded that **8** after localizing in the cytosol of MCF-7 cells and triggered intracellular ROS production and NADH oxidation under light exposure. The ROS production and NADH photo-oxidation would have created oxidative stress and redox imbalance in cancer cells to hamper the

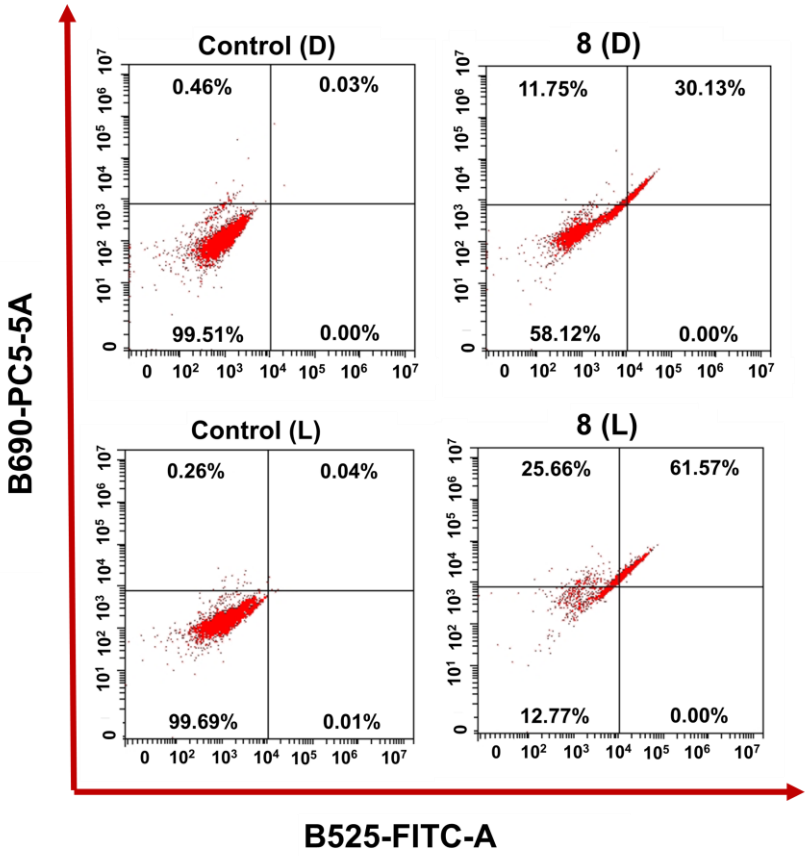

Figure 4.18: Quantitative measurement of caspase 3/7 activation by staining with caspase-3/7 green detection reagent and SYTOX red (L = Light, D = Dark). Incubation time with **8**: 12 h, Light irradiation (400-700 nm, 5.0 J cm^{-2}) for 2 min. Recovery after irradiation: 12 h. For the dark group, the light irradiation step was absent. The experiment was repeated three times independently with similar results.

electron transport chain of mitochondria, further compromising the MMP. This MMP loss would have triggered caspase 3-7 activation to kill the cancer cells *via* the apoptotic cell death mechanism.

4.4. Conclusion

This study effectively synthesized and characterized two novel Ir(III)-based NADH photooxidation photocatalysts, **7** and **8**, demonstrating anticancer potential. Both photocatalysts (**7** and **8**) showed visible light absorbance (400-550 nm) due to MLCT and coumarin 6-based electronic transitions, which allowed them to be used for light-driven catalytic NADH oxidation and anticancer applications. In PBS, **7** showed a turnover number (TON) of *ca*. 97.7±5.7 and a turnover frequency (TOF) of roughly 969.3±56.9 h^{-1}. **8** was even more efficient, exhibiting a TON of *ca*. 108.2±4.2 and a TOF of *ca*. 1084.6±39.4 h^{-1}. **8** demonstrated higher catalytic activity than previously reported green-light Ir(III) photocatalysts.[5,6,12,21] Moreover, **7** and **8** also produced $^{\bullet}OH$, H_2O_2, and $^1O_2$, suggesting their potential to act as both type I and type II ROS generating agents. Furthermore, **7** and **8** demonstrated significantly higher cytotoxicity against MCF-7 and HeLa cells than normal HEK-293 cells (selectivity index up to 22), indicating their selective toxicity towards cancer cells. The anticancer activity of **7** and **8** was also improved in the presence of light (phototoxicity index up to 7). Further, the cell death mechanism in MCF-7 cells revealed that after localizing in the cytosol, photocatalyst **8** induced intracellular ROS generation and NADH oxidation, causing MMP alteration and caspases 3/7 activation to trigger apoptotic cell death under visible light exposure.

4.5. Experimental Section

4.5.1. Materials

2-Acetyl pyridine, $AgNO_3$, and benzaldehyde were purchased from Finar Ltd. (India). HeLa, MCF-7, and HEK-293 cell lines were procured from NCCS Pune, India. The details of the remaining material are provided in **Chapter II** (**section 2.5.1**).

Scheme:

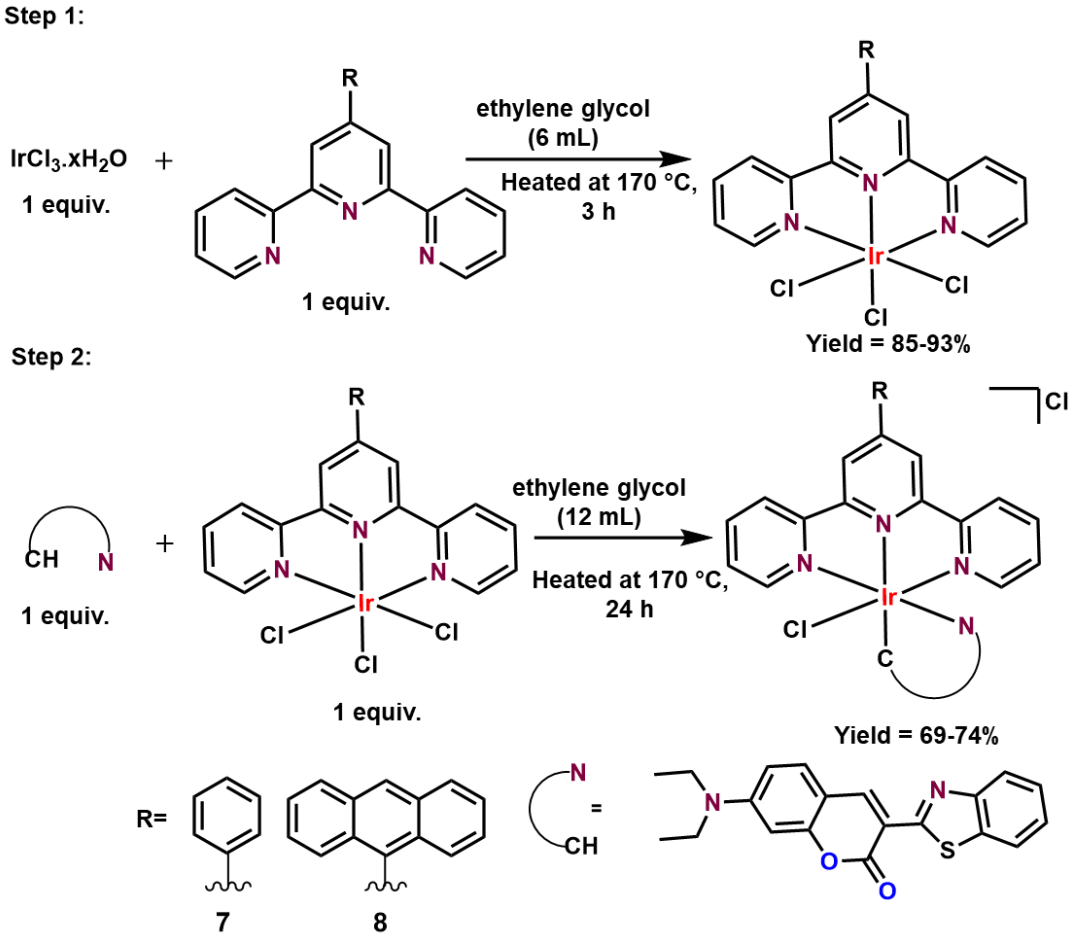

Scheme 4.1: Synthetic scheme for the synthesis of **7** and **8**.

4.5.2. General Synthetic Procedure

4'-phenyl-2,2':6',2''-terpyridine (Ph-tpy), 4'-anthracenyl-2,2':6',2''-terpyridine (An-tpy) were synthesized according to the method described in the literature.[43]

4.5.3. Synthesis of [Ir(Ph/An-tpy)Cl_3]

A mixture of $IrCl_3 \cdot xH_2O$ (1 equiv.) and Ph/An-tpy (1 equiv.) in ethylene glycol (6 mL) was heated at 170 °C for 3 h (Scheme 4.1). After cooling to room temperature, the reddish-brown precipitate of [Ir(Ph/An-tpy)Cl_3] was collected by filtration and washed with water to obtain [Ir(Ph/An-tpy)Cl_3] as a reddish-brown solid in good yield (85-93%).

4.5.4. Synthesis of [Ir(Ph/An-tpy)(CO6)Cl]Cl (**7** and **8**)

Photocatalysts **7** and **8** were obtained by heating [Ir(Ph/An-tpy)Cl_3] (1 equiv.) and coumarin 6 (CO6) (1 equiv.) in ethylene glycol (12 mL) at 170 ºC for 24 h (Scheme 4.1). The reaction mixture was then cooled to ambient temperature, followed by the addition of cold distilled water. Ultimately, the crude precipitate of [Ir(CO6)(Ph-tpy)Cl]Cl (**7**) and [Ir(CO6)(An-tpy)Cl]Cl (**8**) was collected by filtration and washed with water. **7** and **8** were purified by column chromatography in neutral alumina using methanol and ethyl acetate (1:99, v/v) as eluents and obtained as a yellow solid in good yield (69-74%).

Photocatalyst **7**: Yield = 74 %, $C_{41}H_{32}Cl_2IrN_5O_2S$ (MW = 921.92). Elemental analysis: calcd: C = 53.42, H =3.50, N = 7.60, obtained: C = 53.31, H = 3.59, N = 7.81. UV-Vis. spectral data were recorded in DMSO:PBS (0.5:99.5, v/v) where λ_{max} = 479 nm ($\varepsilon = 5.91 \times 10^4\ M^{-1}\ cm^{-1}$), 452 nm ($\varepsilon = 4.47 \times 10^4\ M^{-1}\ cm^{-1}$), 369 nm ($\varepsilon = 3.2 \times 10^4\ M^{-1}\ cm^{-1}$). Emission spectra were recorded in DMSO:PBS (0.5:99.5, v/v) λ_{ex} = 460 nm, λ_{em} = 514 nm. HR-MS

(m/z for $[M]^+$) in MeOH: expected = 886.1594, obtained = 886.2027. ^{1}H NMR (500 MHz, DMSO-d_6, ppm) δ: 9.61 (m, 1H), 9.41 (s, 2H), 9.07 (t, *J* = 10.1 Hz, 2H), 8.44 (d, *J* = 7.5 Hz, 2H), 8.39 (m, 1H), 8.32 (t, *J* = 7.9 Hz, 2H), 7.91 (d, *J* = 5.5 Hz, 2H), 7.79 (t, *J* = 7.6 Hz, 2H), 7.72 (t, *J* = 7.3 Hz, 2H), 7.65 (m, 3H), 6.38 (d, *J* = 2.5 Hz, 1H), 6.28 (d, *J* = 9.3 Hz, 1H), 6.07 (d, *J* = 9.4 Hz, 1H), 3.31 (t, *J* = 6.9 Hz, 4H), 0.97 (m, 6H). ^{13}C NMR (125 MHz, DMSO-d_6, ppm) δ: 161.64, 160.75, 158.45, 157.21, 157.01, 156.64, 154.66, 153.40, 153.25, 152.58, 150.57, 142.92, 141.42, 135.79, 135.32, 132.48, 132.07, 129.90, 129.78, 128.92, 128.55, 126.76, 124.95, 122.39, 122.23, 121.30, 111.04, 110.77, 108.52, 96.64, 44.99, 12.83.

Photocatalyst **8:** Yield = 69 %, $C_{49}H_{36}Cl_2IrN_5O_2S$ (MW = 1022.04). Elemental analysis: calcd: C = 57.58, H = 3.55, N = 6.85, obtained: C = 57.82, H = 3.61, N = 6.72. UV-Vis. spectral data were recorded in DMSO:PBS (0.5:99.5, v/v) where λ_{max} = 477 nm (ε = 9.28 × 10^4 M^{-1} cm^{-1}), 454 nm (ε = 7.61 ×10^4 M^{-1} cm^{-1}), 387 nm (ε = 1.9 ×10^4 M^{-1} cm^{-1}), 368 nm (ε = 6.11 ×10^4 M^{-1} cm^{-1}). Emission spectra were recorded in DMSO:PBS (0.5:99.5, v/v) λ_{ex} = 460, λ_{em} = 512 nm. HR-MS (m/z for $[M]^+$) in MeOH: expected = 986.1907, obtained = 986.2212. ^{1}H NMR (500 MHz, DMSO-d_6, ppm) δ: 9.00 (s, 2H), 8.86 (m, 2H), 8.66 (d, *J* = 3.9 Hz, 1H), 8.49 (s, 1H), 8.23 (d, *J* = 8.1 Hz, 2H), 8.12 (m, 2H), 7.99 (d, *J* = 8.0 Hz, 1H), 7.81 (m, 13H), 6.83 (d, *J* = 8.8 Hz, 1H), 6.65 (s, 1H), 3.49 (d, *J* = 6.9 Hz, 4H), 1.16 (t, *J* = 6.8 Hz, 6H). ^{13}C NMR (125 MHz, DMSO-d_6, ppm) δ: 161.66, 160.77, 157.22, 155.91, 155.27, 152.71, 152.61, 149.85, 149.00, 142.97, 142.93, 138.15, 137.95, 135.83, 131.30, 129.26, 128.20, 123.31, 122.50, 122.32, 122.15, 121.55, 111.03, 110.85, 108.53, 96.74, 44.86.

4.5.5. Instruments

Instrumental details for UV-Vis, fluorescence, HRMS, multinuclear NMR, cell imaging, and FACS analysis are provided in **Chapter II** (**section 2.5.2**).

4.5.6. NMR Spectroscopy

The methods are provided in **Chapter II** (**section 2.5.7**).

4.5.7. UV-Vis. Spectroscopy

The method to record UV-Vis. Spectra are provided in **Chapter II** (**section 2.5.8**). Herein, the DMSO:PBS (0.5:99.5, v/v) is used as a solvent system.

4.5.8. Fluorescence Spectra

The method to record fluorescence spectra of photocatalysts **7** and **8** (20 μM) in DMSO:PBS (0.5:99.5, v/v) solution is given in **Chapter II** (**section 2.5.9**).

4.5.9. Lipophilicity Measurement

The partition coefficient of **7** and **8** was determined through the shake-flask method.[13] To prepare water-saturated octanol, 4 mL of octanol was mixed with 1 mL of water and left for 24 h.[13] Similarly, octanol-saturated water was prepared using a similar procedure.[13] The photocatalyst was then solubilized in 2 mL of saturated octanol by adding a minimal volume of DMSO, and this solution was added to 2 mL of saturated water.[13] The resulting mixture underwent 24 h of shaking using a mechanical shaker, followed by settling and separation. The concentration of the photocatalyst was subsequently assessed through UV-Vis. absorption spectroscopy. The outcome of the results was expressed as mean ± S.D

(sample size = 3) of the three independent repeated experiments. The partition coefficient was calculated by the following equation.

$\log P_{o/w} = \log([\text{photocatalyst}]_{octanol}/[\text{photocatalyst}]_{water})$.

4.5.10. Photo-Stability of Photocatalysts

The method to study the photostability of photocatalysts **7** and **8** in DMSO:PBS (0.5:99.5, v/v) solution under green light irradiation (525 nm, 50.2 J cm^{-2}) is given in **Chapter II** (**section 2.5.10**).

4.5.11. Dehalogenation Study of 7

The solution of photocatalyst **7** (20 μM) and $AgNO_3$ (24 μM) in MeOH was prepared at ambient temperature. UV-Vis. spectra of that solution were recorded after 24 h. In brief, photocatalyst **7** (20 μM) in MeOH was stirred for 24 h with $AgNO_3$ (24 μM) at 60 °C to remove the coordinated chlorine. After filtering out the precipitate of AgCl *via* a syringe filter, the resulting UV peaks for the dehalogenated species were assigned.

4.5.12. Computational Details

The methods to perform the DFT and TD-DFT calculations are given in **Chapter III** (**section 3.5.10**.

4.5.13. Photocatalytic Reactions of 7/8 with NADH

The method for performing the photocatalytic reaction of photocatalysts **7/8** (1 μM each) and NADH (150 μM) in DMSO:PBS (0.5:99.5, v/v) at different time intervals is provided

in **Chapter II** (**section 2.5.11**). The light used in this experiment was 525 nm (50.2 J cm^{-2}).

4.5.14. Photocatalytic Reactions of 8 with NADH in the Presence of GSH (Glutathione)

Reactions between photocatalyst **8** (1 μM), NADH (150 μM), and GSH (50 μM) in DMSO:PBS (0.5:99.5, v/v) at different time intervals were monitored by UV-Vis. Spectroscopy on irradiation with green light (525 nm, 50.2 J cm^{-2}).

4.5.15. Detection of H_2O_2 Generation

In the reaction of photocatalyst **8** (1 μM) with NADH (150 μM) in DMSO:PBS (0.5:99.5, v/v) at ambient temperature in the dark or after light irradiation (525 nm, 50.2 J cm^{-2}), H_2O_2 was detected by Quantofix peroxide test sticks.

4.5.16. Determination of Singlet Oxygen and ˙OH Generation

The method for performing the singlet oxygen generation by photocatalyst **7/8 (**2 μM each**)** is given in **Chapter II** (**section 2.5.13**). The light dose used was 525 nm (50.2 J cm^{-2}). Similarly, the method for performing the ˙OH generation by photocatalyst **7/8 (**2 μM each**)** is given in **Chapter III** (**section 3.5.15**. The light dose used was 525 nm (50.2 J cm^{-2}).

4.5.17. Determination of Hydroxyl Radical Generation in the Presence of ˙OH Scavenger

The production of photo-induced hydroxyl radical (˙OH) by **8** was studied in the presence of ˙OH scavenger (tert-butanol) using the hydroxyl radical sensor methylene blue.[44,45] Briefly, **8** (2 μM) in DMSO:PBS (0.5:99.5, v/v) was mixed with methylene blue (15 μM)

and tert-butanol (8 µL). The solution was then placed in quartz cuvettes, followed by 525 nm (50.2 J cm^{-2}) light irradiation for different times at ambient temperature. The change in absorbance of the methylene blue was then monitored by UV-Vis. spectroscopy.

4.5.18. MTT Assay

A cytotoxicity assessment was conducted on MCF-7, HeLa, and HEK-293 cells to evaluate the cytotoxic impact of **7** and **8** under both dark and light (400-700, 5.0 J cm^{-2}) irradiation by following the protocol given in **Chapter II (section 2.5.14)**.

4.5.19. Cellular Uptake

The cellular uptake study has been done on MCF-7 cells. Briefly, 0.5 x 10^5 cells were seeded in 12-well plates in DMEM with 10% FBS and 1% penicillin-streptomycin solution, and placed in a 37 ℃, 5% CO_2 incubator for 24 h to equilibrate and allow cell attachment. The cells were then treated with **8** at its light IC_{50} value concentration and kept for a 6 h incubation in a 5% humidified CO_2 incubator at 37 ˚C. Prior to imaging, the drug-containing medium was discarded, and 100 µL PBS was added to all wells of the 12-well plates, and images were captured in phase contrast as well as in the green channel at 40X with a 3-second exposure.

4.5.20. In cell NADH Oxidation

The method to perform intracellular photocatalytic NADH oxidation study in the presence of **8** (0.5 µM) are given in **Chapter III (section 3.5.19)**.

4.5.21. Intracellular ROS Generation

The method to study the intracellular ROS by DCFH-DA assay in the presence of **8** (at its light IC_{50} concentration of *ca.* 0.3 μM) is given in **Chapter II (section 2.5.15)**.

4.5.22. JC-1 Assay

The method to study the mitochondrial depolarization by JC-1 assay in the presence of **8** (at its light IC_{50} concentration of *ca.* 0.3 μM) is provided in **Chapter II (section 2.5.16)**.

4.5.23. Apoptosis Study by Hoechst/PI Dual Staining

The method to study the mechanism of cell death by Hoechst/PI Dual Staining in the presence of **8** (at its light IC_{50} concentration of *ca.* 0.3 μM) is provided in **Chapter II (section 2.5.17)**.

4.5.24. Caspase 3/7 Activation Assay

The method for caspase 3/7 activation study in the presence of **8** (at its light IC_{50} concentration of *ca.* 0.3 μM) is provided in **Chapter II (section 2.5.20).**

4.5.25. Statistical Analysis

The outcome of the results was expressed as mean ± standard error of the three independent repeated experiments. Sample size, i.e., n = 3, was used for respective statistical analysis. The statistical analysis was conducted utilizing SPSS 16.0 (SPSS, Chicago, IL, USA) software. Results were compared between the dark control and the rest of the group (**8**, Control (Light), and **8**+Light). The statistical analysis was done by One-way ANOVA

followed by Tukey's Post Hoc Test. Values of $p<0.05$ were considered statistically significant.

References:

1. A. K. Yadav, A. Upadhyay, A. Bera, R. Kushwaha, A. A. Mandal, S. Acharjee, A. Kunwar, S. Banerjee, *Inorg. Chem. Front*. **2024**, *11*, 5435-5448.
2. S. Ghosh, P. Paira, *Eur. J. Inorg. Chem.* **2025**, *28*, e202400769.
3. Z. Fan, J. Xie, R. Kushwaha, S. Liang, W. Li, A. A. Mandal, L. Wei, S. Banerjee, H. Huang, *Chem. Asian J.* **2023**, *18*, e202300047.
4. A. K. Yadav, V. Singh, R. Kushwaha, A. Kunwar, B. Koch, S. Banerjee, *Inorg. Chem. Commun.* **2025**, *175*, 114184.
5. Z. Fan, Y. Rong, T. Sadhukhan, S. Liang, W. Li, Z. Yuan, Z. Zhu, S. Guo, S. Ji, J. Wang, R. Kushwaha, S. Banerjee, K. Raghavachri, H. Huang, *Angew. Chem. Int. Ed*. **2022**, *61*, e202202098.
6. H. Huang, S. Banerjee, K. Qiu, P. Zhang, O. Blacque, T. Malcomson, M. J. Paterson, G. J. Clarkson, M. Staniforth, V. G. Stavros, G. Gasser, H. Chao, P. J. Sadler, *Nat. Chem*. **2019**, *11*, 1041-1048.
7. C. Huang, C. Liang, T. Sadhukhan, S. Banerjee, Z. Fan, T. Li, Z. Zhu, P. Zhang, K. Raghavachari, H. Huang, *Angew. Chem. Int. Ed.* **2021**, *60*, 9474-9479.
8. Z. Fan, J. Xie, T. Sadhukhan, C. Liang, C. Huang, W. Li, T. Li, P. Zhang, S. Bane rjee, K. Raghavachari, H. Huang, *Chem. Eur. J*. **2022**, *28*, e202103346.
9. W. Wu, W. Wu, S. Ji, H. Guo, J. Zhao, *Dalton Trans*. **2011**, *40*, 5953-5963.
10. C. Li, W. Lu, X. Zhou, M. Pang, X. Luo, *Anal. Chem*. **2018**, *90*, 14239-14246.

11. S. Bonnet, *J. Am. Chem. Soc*. **2023**, *145*, 23397-23415.

12. Y. Yang, Y. Gao, J. Zhao, S. Gou, *Inorg. Chem. Front*. **2024**, *11*, 436-450.

13. V. Novohradsky, A. Marco, L. Markova, N. Cutillas, J. Ruiz, V. Brabec, *J. Med. Chem*. **2023**, *66*, 9766-9783.

14. T. W. Johnson, R. A. Gallego, M. P. Edwards, *J. Med. Chem.* **2018**, *61*, 6401-6420.

15. A. Rilak, I. Bratsos, E. Zangrando, J. Kljun, I. Turel, Z. D. Bugarcic, E. Alessio, *Inorg. Chem*. **2014**, *53*, 6113-6126.

16. M. M. Milutinovic, A. Rilak, I. Bratsos, O. Klisuric, M. Vranes, N. Gligorijevic, S. Radulovic, Z. D. Bugarcic, *J. Inorg. Biochem*. **2017**, *169*, 1-12.

17. L. Wei, R. Kushwaha, A. Dao, Z. Fan, S. Banerjee, H. Huang, *Chem. Commun*. **2023**, *59*, 3083-3086.

18. Z. Zhu, L. Wei, Y. Lai, W. L. O. Carter, S. Banerjee, P. J. Sadler, H. Huang, *Dalton Trans*. **2022**, *51*, 10875-10879.

19. Gaussian 16, Revision A.03, M. J. Frisch, G. W. Trucks, H. B. Schlegel, G. E. Scuseria, M. A. Robb, J. R. Cheeseman, G. Scalmani, V. Barone, G. A. Petersson, H. Nakatsuji, X. Li, M. Caricato, A. V. Marenich, J. Bloino, B. G. Janesko, R. Gomperts, B. Mennucci, H. P. Hratchian, J. V. Ortiz, A. F. Izmaylov, J. L. Sonnenberg, D. Williams-Young, F. Ding, F. Lipparini, F. Egidi, J. Goings, B. Peng, A. Petrone, T. Henderson, D. Ranasinghe, V. G. Zakrzewski, J. Gao, N. Rega, G. Zheng, W. Liang, M. Hada, M. Ehara, K. Toyota, R. Fukuda, J. Hasegawa, M. Ishida, T. Nakajima, Y. Honda, O. Kitao, H. Nakai, T. Vreven, K. Throssell, J. A. Montgomery, Jr., J. E. Peralta, F. Ogliaro, M. J. Bearpark, J. J. Heyd, E. N. Brothers, K. N. Kudin, V. N. Staroverov, T. A. Keith, R. Kobayashi,

J. Normand, K. Raghavachari, A. P. Rendell, J. C. Burant, S. S. Iyengar, J. Tomasi, M. Cossi, J. M. Millam, M. Klene, C. Adamo, R. Cammi, J. W. Ochterski, R. L. Martin, K. Morokuma, O. Farkas, J. B. Foresman, and D. J. Fox, Gaussian 16, Inc., Wallingford CT, **2016**.

20. X. Cui, J. Fan, Y. Gao, X. Zhou, C. Zhang, Q. Meng, *J. Med. Chem*. **2024**, *67*, 19826-19836.
21. Z. Zhu, L. Wei, Y. Lai, W. L. O. Carter, S. Banerjee, P. J. Sadler, H. Huang, *Dalton Trans*. **2022**, *51*, 10875-10879.
22. L. Qiao, J. Liu, S. Kuang, X. Liao, J. Kou, L. Ji, H. Chao, *Dalton Trans*. **2021**, *50*, 14332-14341.
23. A. Bera, S. Gautam, S. Sahoo, A. K. Pal, P. Kondaiah, A. R. Chakravarty, *RSC. Med. Chem*. **2022**, *13*, 1526-1539.
24. A. A. Mandal, V. Singh, S. Saha, S. Peters, T. Sadhukhan, R. Kushwaha, A. K. Yadav, A. Mandal, A. Upadhyay, A. Bera, A. Dutta, B. Koch, S. Banerjee, *Inorg. Chem*. **2024**, *63*, 7493-7503.
25. Y. Dong, C. Feng, P. Jiang, G. Wang, K. Li, H. Miao, *RSC Adv*. **2014**, *4*, 7340-7346.
26. J. Jiang, H. Li, L. Zhang, *Chem. Eur. J*. **2012**, *18*, 6360-6369.
27. R. T. Ryan, K. C. Stevens, R. Calabro, S. Parkin, J. Mahmoud, D. Y. Kim, D. K. Heidary, E. C. Glazer, J. P. Selegue, *Inorg. Chem*. **2020**, *59*, 8882-8892.
28. S. Liu, J. Han, W. Wang, Y. Chang, R. Wang, Z. Wang, G. Li, D. Zhu, M. R. Bryce, *Dalton Trans*. **2022**, *51*, 16119-16125.

29. J. Karges, S. Kuang, F. Maschietto, O. Blacque, I. Ciofini, H. Chao, G. Gasser, *Nat. Commun.* **2020**, *11*, 3262.

30. J. V. Meerloo, G. J. Kaspers, J. Cloos, *Methods Mol. Biol*. **2011**, *731*, 237-245.

31. N. P. Bigham, J. J. Wilson, *Eur. J. Inorg. Chem*. **2023**, *26*, e202200735.

32. S. E. Burdall, A. M. Hanby, M. R. J. Lansdown, V. Speirs, *Breast Cancer Res*. **2003**, *5*, 89-95.

33. B. Joshi, M. Shivashankar, *ACS Omega* **2023**, *8*, 43408-43432.

34. B. Kar, U. Das, N. Roy, P. Paira, *Coord. Chem. Rev*. **2023**, *474*, 214860.

35. S. Nikolić, J. Arakelyan, V. Kushnarev, S. M. Alfadul, D. Stanković, Y. I. Kraynik, S. G. Šipka, M. V. Babak, *Inorg. Chem*. **2023**, *62*, 8188-8199.

36. A. C. Carrasco, V. R. Fanjul, A. Habtemariam, A. M. Pizarro, *J. Med. Chem*. **2020**, *63*, 4005-4021.

37. D. G. Nicholls, M. W. Ward, *Trends Neurosci*. **2000**, *23*, 166-174.

38. M. Reers, T. W. Smith, L. B. Chen, *Biochem.* **1991**, *18*, 4480-4486.

39. S. P. Vaidya, M. Patra, *Curr. Opin. Chem. Biol*. **2023**, *72*, 102236.

40. G. Sharma, N. K. Rana, P. Singh, P. Dubey, D. S. Pandey, B. Koch, *Biomed. Pharmacother*. **2017**, *88*, 218-231.

41. P. Goswami, V. Singh, B. Koch, *J. Ethnopharmacol*. **2024**, *334*, 118537.

42. H. R. Stennicke, J. M. Jurgensmeier, H. Shin, Q. Deveraux, B. B. Wolf, X. Yang, Q. Zhou, H. M. Ellerby, L. M. Ellerby, D. Bredesen, *J. Biol. Chem*. **1998**, *273*, 27084-27090.

43. J. Wang, G. S. Hanan, *Synlett* **2005**, *8*, 1251-1254.

44. Y. Dong, C. Feng, P. Jiang, G. Wang, K. Li, H. Miao, *RSC Adv*. **2014**, *4*, 7340-7346.

45. J. Jiang, H. Li, L. Zhang, *Chem. Eur. J.* **2012**, *18*, 6360-6369.